

RESEARCH ARTICLE

Neural Circuits

Inferring thalamocortical monosynaptic connectivity in vivo

Yi Jun Liew,^{1,3}  Aurélie Pala,¹  Clarissa J. Whitmire,¹  William A. Stoy,¹ Craig R. Forest,² and
 Garrett B. Stanley¹

¹Wallace H. Coulter Department of Biomedical Engineering, Georgia Institute of Technology and Emory University, Atlanta, Georgia; ²George W. Woodruff School of Mechanical Engineering, Georgia Institute of Technology, Atlanta, Georgia; and ³Joint PhD Program in Biomedical Engineering, Georgia Institute of Technology–Emory University–Peking University, Atlanta, Georgia

Abstract

As the tools to simultaneously record electrophysiological signals from large numbers of neurons within and across brain regions become increasingly available, this opens up for the first time the possibility of establishing the details of causal relationships between monosynaptically connected neurons and the patterns of neural activation that underlie perception and behavior. Although recorded activity across synaptically connected neurons has served as the cornerstone for much of what we know about synaptic transmission and plasticity, this has largely been relegated to *ex vivo* preparations that enable precise targeting under relatively well-controlled conditions. Analogous studies *in vivo*, where image-guided targeting is often not yet possible, rely on indirect, data-driven measures, and as a result such studies have been sparse and the dependence upon important experimental parameters has not been well studied. Here, using *in vivo* extracellular single-unit recordings in the topographically aligned rodent thalamocortical pathway, we sought to establish a general experimental and computational framework for inferring synaptic connectivity. Specifically, attacking this problem within a statistical signal detection framework utilizing experimentally recorded data in the ventral-posterior medial (VPM) region of the thalamus and the homologous region in layer 4 of primary somatosensory cortex (S1) revealed a trade-off between network activity levels needed for the data-driven inference and synchronization of nearby neurons within the population that results in masking of synaptic relationships. Here, we provide a framework for establishing connectivity in multisite, multielectrode recordings based on statistical inference, setting the stage for large-scale assessment of synaptic connectivity within and across brain structures.

NEW & NOTEWORTHY Despite the fact that all brain function relies on the long-range transfer of information across different regions, the tools enabling us to measure connectivity across brain structures are lacking. Here, we provide a statistical framework for identifying and assessing potential monosynaptic connectivity across neuronal circuits from population spiking activity that generalizes to large-scale recording technologies that will help us to better understand the signaling within networks that underlies perception and behavior.

causality; cross correlation; inference; signal detection; thalamocortical circuit

INTRODUCTION

Every aspect of brain function, from sensory and motor processing to memory and cognition, involves complex circuitry and communication across many different brain areas. Despite this fact, what we know about brain function has been derived largely from electrophysiological recordings targeted at single regions and upon gross anatomical connection patterns across brain regions without specific precise knowledge of synaptic connectivity. Ultimately, understanding the causal

interaction of neuronal dynamics that underlie perception and behavior requires “ground truth” evidence for synaptic connectivity that necessitates intracellular access to both pre- and postsynaptic neurons. Despite exciting advancement of a range of recording technologies such as simultaneous multineuron intracellular recordings *in vivo* (1, 2) and deep structure-targeted patching (3), targeting connections *in vivo* with intracellular approaches remains a labor-intensive endeavor, is ultimately limited to a very small number of neurons, and does not scale to the circuit level. Extracellular



recordings offer solutions to some of these issues and thus offer promise in this direction.

The field of neuroscience is now at a time when large-scale recordings of neuronal populations at cellular resolution are possible across brain structures because of the development of multielectrode recording technologies such as NeuroNexus (4, 5) (NeuroNexus Inc.), “Neuropixels” (6), NeuroSeeker (7, 8), and three-dimensional (3-D) silicon probes (9). These technologies provide access to surveying network-level information flow, driving a growing need for a rigorous experimental and analytic framework to identify functional relationships across brain structures. In previous studies, *in vivo* approaches to establishing synaptic connectivity across recorded pairs of neurons have been developed based on analytic methods applied to recorded spiking data (10, 11), historically conducted in larger animals such as cats, rabbits, and rats (12–14) and only more recently in mice (15). Approaches based on spike correlations are the most common for quantifying functional interactions and inferring monosynaptic connections *in vivo*. These approaches have been utilized in paired recording studies that involved measuring correlation in the spiking activity between neurons (12–14, 16–19) or between the spiking activity of a presynaptic neuron and the subthreshold membrane potential of a putative postsynaptic target (20–24). Correlational approaches are statistical in nature and thus have been anecdotally reported to be strongly dependent upon data length and are very sensitive to a range of possible confounds, but a comprehensive understanding of these relationships and a unified approach are both lacking.

Here, using the thalamocortical circuit in rodents as a model system, we establish methodological strategies for extracellular, topographically aligned *in vivo* single-unit recordings in thalamus and cortex for both rat and mouse. This analytic framework for inferring connectivity is based on signal detection theory and directly addresses issues of data length dependence and confounds produced by population synchrony. Specifically, we outline a workflow of topographic mapping and histological validation, followed by a statistical approach for signal detection-based classification of putative connected and nonconnected pairs with an assessment of classification confidence that is scalable to the large-scale recording approaches that are emerging in the field. We found that although the amount of spiking was a strong determinant of the accuracy of the inference of connectivity, there was an important trade-off between the activity in the network and the underlying population synchrony that regulates the likelihood of both discovering a synaptic connection that is present and correctly classifying unconnected pairs as such. Taken together, this provides a data-driven framework for inferring connectivity and the corresponding statistical confidence that generalizes to large-scale recordings across brain structures.

METHODS

Animals

Twelve adult female Sprague–Dawley rats (no age restriction, 225–330 g) and four adult male C57BL/6 mice (8–16 wk, 25–35 g) were used in all the experiments. All procedures

were approved by the Georgia Institute of Technology Institutional Animal Care and Use Committee and followed guidelines established by the National Institutes of Health. Note that there were some major differences in animal preparation, surgery, and craniotomies as well as electrophysiology for rat and mouse, as described below. However, procedures such as whisker stimulation, postmortem histology, and analytical methods used for analysis were largely identical.

Animal Preparation, Surgery, and Craniotomies

Rat.

Animals were first sedated with 5% vaporized isoflurane and maintained at 3% vaporized isoflurane when transitioned to fentanyl cocktail anesthesia via tail vein injection. Fentanyl cocktail anesthesia [fentanyl (5 μ g/kg), midazolam (2 mg/kg), and dexmedetomidine (150 mg/kg)] was administered continuously via a drug pump at an initial rate of 4.5 μ L/min (25, 26). During the transition, anesthesia level was monitored closely by measurement of heart rate and respiratory rate. Body temperature was maintained at 37°C by a servo-controlled heating pad. Under the effect of both anesthetic agents, the animal’s heart rate tended to decrease gradually over several minutes. The isoflurane level was then titrated down in 0.5% decrements during the transition to the fentanyl cocktail. Upon successful transition, which ranged from 5 to 15 min depending on the animal, the heart rate was targeted for ~240–270 beats/min. After the effects of fentanyl cocktail stabilized (in terms of heart rate) and the animals showed no toe pinch response, the animals were then fixed in the stereotaxic device by securing the head of the animal in place with ear bars on a floating table in an electromagnetically shielded surgery suite. The position of the ear bars was verified with uniform eye levels and usually with eardrum penetration on both sides of the head. Eye ointment (Puralube Vet Ointment) was applied to prevent dehydration of the animal’s eyes. An incision was made along the midline of the skull, and skin was removed for visibility of bregma and lambda (27). Connective tissue and muscle that were close to the ridge of the skull were detached and removed to expose the skull surface that was directly above the barrel cortex. To ensure that the skull remained level throughout the recording, the height of the skull surface was measured at bregma and lambda, and the difference was minimized (<200 μ m) by adjusting the angle of the head with the nose cone position.

We made two craniotomies on the animal’s left hemisphere above the ventro-posteromedial nucleus (VPm) and the primary somatosensory cortex (S1) barrel cortex based on stereotaxic coordinates. For the cortical craniotomy, which usually extended over the ridge of the skull, the stereotaxic device was rotated to an angle (~40° relative to vertical) for better visualization and drilling. Both craniotomies were drilled slowly until the skull piece appeared to be floating and mobile. We irrigated the skull surface periodically with Ringer solution when drilling to remove debris and prevent overheating from the drilling. Before removal of the skull piece to expose the cortex, a small dental cement reservoir was carefully built around the craniotomies to hold the Ringer solution for irrigation and to keep the recording site

continually moist. The lateral side of the wall was built thicker and higher because of the curvature of the skull toward the ridge. To provide strong adherence to the skull, cyanoacrylate-containing adhesive (Krazy Glue, Elmer's Products Inc.) was carefully applied around the external edges of the reservoir, leaving the bregma and major skull sutures visible at all times. For grounding purposes, another hole with ~0.5-mm diameter was drilled (Henry Schein, Carbide Burr HP 2) on the right hemisphere of the skull and fastened with a skull screw and a metal wire. The skull pieces at both recording sites were then carefully removed with forceps (FST Dumont #5/45). To minimize brain swelling, the dura was left intact on both recording surfaces, and warm Ringer solution was repeatedly added and absorbed with cotton tips until the blood was cleared. An absorbent gelatin compressed sponge (Gelfoam, Pfizer Inc.) was sometimes used to clear the blood.

Mouse.

Headplate implantation and intrinsic imaging procedure were usually performed at least 3 days to 1 wk before acute experiments. A lightweight custom metal (titanium or stainless steel) headplate was implanted on the skull of the mouse for head fixation and improved stability during recording, in accordance with a previously described protocol (28). During this survival surgical preparation, the animal was sedated with 5% vaporized isoflurane and anesthesia was maintained with 2–3% isoflurane for the headplate procedure. We administered opioid and nonsteroidal anti-inflammatory analgesic (buprenorphine SR 0.8–1 mg/kg sc preoperatively and ketoprofen 5–10 mg/kg ip postoperatively) and covered the animal's eyes with ophthalmic eye ointment (Puralube Vet Ointment). Body temperature was monitored and maintained at 37°C. After sterilizing the skin above the skull and applying topical anesthetic (lidocaine 2%, 0.05 mL, max 7 mg/kg sc), we removed the skin and scraped off periosteum and any conjunctive tissue from the skull. We gently separated tissue and muscles close to the lateral edge of the skull with a scalpel blade (Glass Van & Technocut, size no. 15), leaving sufficient room for headplate attachment and away from targeted recording areas. To ensure that the skull surface remained level during head fixation, we adjusted the animal's head position to minimize the relative height difference (<150 μm) between the skull surface at the bregma and lambda landmarks (29). We found this step to be critical especially for VPM targeting. We secured the metal headplate over the intact skull with C&B Metabond (Parkell Products Inc.) and skin adhesive (Loctite 401, Henkel). The Metabond dental acrylic was chilled with ice, slowly applied to the skull surface, and allowed to cure for 5–10 min before we covered the rest of the attachment site and edges of the skin incision with skin adhesive (Loctite 401) to ensure that the skin edges were securely adhered to the skull. The final headplate and dental acrylic structure created a recording well for holding Ringer solution (in mM: 135 NaCl, 5 KCl, 5 HEPES, 1 MgCl₂·6H₂O, 1.8 CaCl₂·2H₂O, pH 7.3) for future imaging and electrophysiological recording sessions. For grounding purposes, another hole with ~0.5-mm diameter was drilled (Henry Schein, Carbide Burr HP 2) on the right hemisphere of the skull and fastened with a skull screw (Miniature Self-Tapping Screws, J. I. Morrisco). A metal wire

was connected to the skull screw on the day of recording to serve as animal ground. We applied a thin layer of transparent glue (Loctite 401, Henkel) over the left hemisphere to protect the skull and covered the exposed skull with a silicone elastomer (Kwik-Cast, World Precision Instruments) if there were no other additional procedures after headplate implantation.

Intrinsic optical imaging in the mouse S1 barrel cortex.

We performed intrinsic signal optical imaging of whisker-evoked responses in mouse primary somatosensory cortex under 1–1.2% isoflurane anesthesia to functionally identify individual barrel columns (30, 31). All whiskers except the whiskers of interest (A2, B1, C2, D1, D3, and E2) were trimmed. We thinned the skull with a dental drill (0.1-mm-diameter bit, Komet USA) until blood vessels became visible. We applied warm Ringer solution on top of the skull and covered it with a glass coverslip (thickness 0.13–0.17 mm, Fisherbrand). We captured a reference image of the blood vasculature under green illumination (530 nm) (M530F1 LED, Thorlabs). We delivered repetitive whisker stimuli (10 Hz, sawtooth pulses, 1,000°/s) to individual whiskers with a galvanometer system (Cambridge Technologies) while performing imaging on barrel cortex under red illumination (625 nm) (M625F1 LED, Thorlabs)(see Whisker Stimulation). Images were acquired with a CCD Camera (MiCam02HR, SciMedia) at 10 Hz, with a field of view of ~4 × 2.5 mm, corresponding to 384 × 256 pixels (resolution: 100 pixels/mm). Each trial lasted 10 s, with 4 s of baseline followed by 4 s of whisker stimulation and 2 s without stimulation. The inter-trial interval was 30 s. Whisker-evoked responses were averaged over 10–20 trials. Intrinsic signals were measured as the relative change in reflectance by taking the overall mean reflectance during whisker stimulation (R_{stim}) and subtracting the mean baseline reflectance ($R_{stim} - R_{baseline}$). Acquisition and processing of the images were implemented with BV_Ana software (MiCam02HR, SciMedia, Ltd) and MATLAB (2015; MathWorks, Natick, MA). We recorded intrinsic signals from at least three barrels and estimated location of the unmapped barrels by overlaying a template barrel map reconstructed from histology. At the end of the imaging session, we applied transparent glue (Loctite 401) directly on the S1 site to protect the thinned skull from contamination and infection and sealed the exposed skull with a silicone elastomer (Kwik-Cast, World Precision Instruments).

On the day of recording, the head of the mouse is held in place with a head-post clamp and the animal should remain in the flat skull position. We covered the eyes with ophthalmic eye ointment (Puralube Vet Ointment) to prevent dehydration. The animal was then anesthetized with 2–3% isoflurane. Before performing the craniotomies, we thinned the skull above VPM and S1 layer by layer with a dental drill (0.1-mm-diameter bit, Komet USA) and irrigated the skull surface with Ringer solution frequently to remove debris and prevent overheating. When the skull was thin enough to easily puncture, we made two small craniotomies above VPM (~1-mm diameter; centered at 1.8 mm caudal and 1.8 mm lateral to bregma) and S1 (~0.5-mm diameter, using the intrinsic imaging signal and the blood vasculature as a landmark) by penetrating the thinned skull with an insulin syringe needle tip (at ~40–50° angle) to make small holes outlining the

edges of the craniotomies until the circular skull piece was loosely attached. The less perforated region of the circular skull piece was used as a pivot, and we levered the skull pieces off from the more perforated edge, using fine-tip forceps (FST Dumont #5SF) to expose the brain surface.

Electrophysiology

Neuronal recordings.

Tungsten microelectrodes (FHC, impedance 2–5 M Ω , 75 μ m in diameter) were used in thalamus and cortex to isolate single units that were responding to a single primary whisker on the contralateral side of the face. Multielectrode silicon probes with 32 recording sites (A1x32-Poly3-5mm-25s-177 or A1x32-Poly3-10mm-50s-177, NeuroNexus) were also independently lowered into the thalamus and cortex. To improve signal quality, we electroplated the silicon probes with the polymer PEDOT:PSS (83) with a nanoZ device (Multi Channel Systems, Germany). The impedances of the contact sites were measured before each recording and ranged from 0.3 to 0.8 M Ω . After each use, the contact sites were soaked in 20% Contrad (labware detergent) overnight for cleaning, and the impedances usually returned to the initial values (0.3–0.8 M Ω). The impedances for the silicon probes were always measured before a recording session, and contact sites that were defective usually showed large fluctuations in raw voltage traces; signals detected at these sites were excluded from analysis before spike sorting. Note that tungsten microelectrodes were used in rat studies and probe recordings were used in mouse studies. Data were collected with a 64-channel electrophysiological data acquisition system (TDT model, etc., RZ2 Bioprocessor). Neuronal signals were amplified, band-pass filtered (500 Hz to 5 kHz), and digitized at \sim 25 kHz per channel. Stimulus waveform and other continuous data were digitized at 10 kHz per channel. Simultaneously, the local field potential (LFP) signals were obtained by using a 0.5- to 200-Hz band-pass filter. The LFPs were used to identify primary whisker response (see Whisker Stimulation).

Rat.

VPM RECORDINGS. We targeted the VPM region of the thalamus by advancing a single tungsten microelectrode (FHC, 2 M Ω impedance) perpendicular to the pial surface into the thalamic craniotomy centered at 3.0 mm caudal and 3.0 mm lateral to bregma. We quickly advanced (\sim 50 μ m/s) to the depth of 4,000 μ m and slowed down to the speed of \sim 3 μ m/s while searching for responsive cells by manually deflecting the whisker on the contralateral side of the vibrissal pad. Whisker-responsive cells were typically located at a depth of 4,800–5,300 μ m, measured with a precision micromanipulator (Luigs & Neumann, Germany).

S1 RECORDINGS. Centering at a position 5.8 mm lateral and 2.5 mm caudal to bregma, we inserted a single tungsten microelectrode at an angle of 40–45° (relative to vertical axis of electrode holder). We positioned the tip of the electrode gently touching the dura and advanced slowly to create an opening in the membrane. The microelectrode was then slowly advanced into cortical tissue at a speed of \sim 3 μ m/s (measured at 1- μ m resolution). All cortical units were recorded at stereotaxic depths of 700–

1,000 μ m, corresponding to layer IV of rat barrel cortex based on the literature (20, 32).

Mouse.

VPM RECORDINGS. For first penetration, electrode was typically lowered at 1.8 mm caudal and 1.8 mm lateral to bregma. If we could not functionally locate VPM by this method, we used the relative distance from the location of barrel cortex (usually measured 1.0–1.2 mm from the B1 or beta barrel column to find whisker-responsive thalamic regions). For probe recordings, we searched for whisker-responsive cells by manual whisker deflection, using the deepest channel as reference. We typically found that whisker-responsive cells were at a depth between 2,800 and 3,200 μ m.

S1 RECORDINGS. Based on intrinsic imaging signal, a small craniotomy (diameter \sim 0.5 mm) was created at the desired location on the barrel cortex that was distant from blood vessels. We positioned the electrode at a 35° angle from the vertical axis (parallel to the barrel column) and recorded from cortical neurons at a stereotaxic depth of 100–750 μ m from the cortical surface.

Whisker Stimulation

To identify the single whisker of interest, we first manually deflected all whiskers on the vibrissal pad while monitoring the extracellular signal. Once units were isolated by moving the electrode as close as possible to the responsive cells that primarily responded to a single whisker, we delivered controlled single-whisker stimulation in the rostral-caudal plane with a computer-controlled actuator galvo-motor (galvanometer optical scanner model 6210H, Cambridge Technology). Whiskers were trimmed \sim 12 mm from the face. Primary whisker (PW) was defined as whisker deflection that evoked the maximal neuronal response with shortest latency (see *Transient stimulus*). The primary whisker was fed into the insertion hole at the end of an extension tube (inner diameter: \sim 200–300 μ m, length: 15 mm) that was connected to the rotor of the galvanometer stimulator. The stimulus probe was positioned at 10 mm from the vibrissal pad. The range of motion of the galvanometer was \pm 20°, with a bandwidth of 200 Hz. The galvanometer system was controlled with a custom-developed hardware/software system (MATLAB Real-Time Simulink System, MathWorks). Whisker-evoked responses were measured with raster plots and peristimulus time histograms (PSTHs, 1-ms bin resolution) across trials.

Transient stimulus.

For mapping whisker receptive field at the recording sites, we presented high-velocity (600 or 1,000°/s) rostral-caudal whisker deflection to evoke reliable whisker responses. Trains of solo pulses, followed by a separate, pulsatile adapting stimulus at 8–10 Hz (26, 28), were delivered 60–100 times. To measure whisker response to different stimulus strength, pulses with angular deflection velocities of 50, 125, 300, 600, 900, and 1,200°/s were presented randomly. Rostral-caudal pulse deflections were either a Gaussian-shaped deflection waveform or a simple exponential sawtooth (rise and fall time = 8 ms). We quantified whisker-evoked activity 30 ms after stimulus onset and then further

characterized onset latencies of first spike within the response window in response to nonadapting solo pulses and adapting pulsatile stimuli over 60–100 trials. Mean first spike latencies (FSLs) were defined as the average time delay between stimulus onset and the first spike in the response window after stimulus presentation. This metric was used for all thalamic and cortical units. For 32-channel probe recording in thalamus, we quantified the LFP response in a 30-ms poststimulus window for each channel to identify principal whiskers (PWs). Well-isolated single units that showed whisker responsiveness were verified by calculating LFP peak amplitude and peak latency to different whisker stimulation.

A neuronal pair was verified to be topographically aligned when they shared 1) maximum response [single unit (SU) max firing rate (FR) and LFP amplitude] to the same primary whisker under punctate stimulation and 2) latency difference of whisker response within 1–5 ms delay (LFP peak latency and SU mean FSL, or SU mean peak latency).

Weak sinusoidal stimulus.

For monosynaptic connection quantification, we probed the thalamocortical circuit, using a weak, desynchronizing sinusoidal whisker stimulus to elevate baseline firing rates in recorded units. We delivered 4°, 2- to 4-Hz weak sinusoidal deflections (14, 20, 33) for ~200–500 trials to obtain at least 2,000 spikes for the cross correlation analysis. Occasionally, we eliminated the first 0.5–1 s of the trials because of high firing rate at the onset of stimulus presentation.

Postmortem Histology

To verify recording sites and the angle of penetration that was optimal for locating VPM and S1, we perfused a small subset of animals after the paired recording experiment. To label each electrode recording track, we slowly retracted the electrode along its axis of entry at the conclusion of recording and applied a few drops of DiI (2.5 mg/mL, in ethanol). We then reinserted the electrode into the same penetration site and back along the same axis and left the electrode in the brain for at least 15 min. After the end of the experiment, we euthanized the animal with an overdose of pentobarbital sodium (Euthasol; 0.5 mL at 390 mg/mL for rat, 0.1 mL at 390 mg/mL for mouse), performed a transcardial perfusion, extracted the brain, and fixed the brain in 4% paraformaldehyde (PFA, Electron Microscopy Sciences) overnight. We sliced the brain into 100- μ m coronal sections and performed cytochrome oxidase (CO) staining to reveal VPM (barreloid) and S1 (barrel). As an additional verification of recording site, we identified the overlap between the DiI-stained recording track and the CO-stained regions.

Analytical Methods

Extracellular spike sorting.

In assessing potential synaptic connectivity by cross correlation analysis, the clear isolation of single-unit activity from extracellularly recorded voltage signals is particularly critical. In all of our paired recording experiments, we performed extracellular single-unit recordings with either tungsten microelectrodes or 32-channel NeuroNexus probes. Although similar in approach, the sorting of recorded data into clusters was implemented with

different software. For the single microelectrodes, we performed spike sorting off-line with the Plexon Offline Sorter (Plexon Inc., Dallas TX), whereas for the 32-channel probe recordings we utilized the Kilosort2 software package (<https://github.com/MouseLand/Kilosort2>) (34). For high-density probe recordings, there was an additional manual curation step using phy (<https://github.com/cortex-lab/phy>) where we refined the output of automatic algorithm and determined whether merging or splitting of specific clusters was necessary based on refractory violation, waveform shape, as well as cross correlogram between clusters. For both tungsten microelectrode and high-density probe recordings, we classified the clusters as single units or multiunits on the basis of the signal-to-noise ratio (SNR) and interspike interval (ISI) distribution. We only included well-isolated clusters for further analysis. The selection of well-isolated clusters, or single units, was based on two criteria: 1) high SNR of the spike waveform [peak-to-peak amplitude (Vpp) of spike waveforms > 3 standard deviations (SDs) of the waveform] and 2) a clear refractory period (35, 36). We defined a single unit as well isolated if it had SNR > 3, ISI violation < 1% for cortical unit and 2% for thalamic unit, and spike waveform with a Vpp > 60 μ V. Given that the spikes of the same neuron were usually detected on multiple sites of a 32-channel probe, the Vpp and SD of the waveform were computed with the channel that had the largest amplitude of spike waveform.

VPM unit verification.

It is important to distinguish different thalamic nuclei from one another, and particularly so in the mouse, where the regions are very small and very close together. After recording, we used a combination of measures to classify thalamic units as VPM: 1) average first spike latency to punctate (non-adapting) stimuli, quantifying the average time between stimulus onset and the first spike fired during the neural response window (30 ms after stimulus onset) (37); 2) shift in average first spike latency response to adapting stimuli, defined as the time difference between average response to the first adapting stimulus and last adapting stimulus (38); and 3) response reliability, defined as the percentage of trials where a response was detected within 20 ms to repetitive stimulation (8–10 Hz) (39). We excluded thalamic units with average first spike latency of >12 ms (Supplemental Fig. S2A; see <https://doi.org/10.6084/m9.figshare.14393570.v1>), latency shift of >20 ms, or response reliability of <20%.

Cortical unit classification.

It was known that S1 layer IV is the major thalamocortical recipient from VPM projections, and there exists some heterogeneity in terms of cortical cell types in layer IV (33). Here, we classified cortical units into fast-spiking units (FSUs) and regular-spiking units (RSUs) by using waveform parameters. We quantified the time interval between trough and peak (t_{12p}) of the spike waveform (16).

Cross correlation analysis.

All analysis was performed on a trial-by-trial basis. Given a spike in a “reference” neuron, we computed the relative times of the spikes from a “target” neuron that occurred within a 25-ms window before and after each reference spike.

Cross correlograms were constructed with a 0.5-ms bin. Traditionally, monosynaptic interactions were known to produce short-latency peaks in the cross correlograms. The latency of the monosynaptic peak within cross correlograms was typically reported to center around 2.5 ms, estimated from thalamocortical excitatory postsynaptic potentials (EPSPs) and spiking activity (12, 13, 20, 23, 33, 40–44). To ensure that our analysis captures correlation from monosynaptic delays only, we allowed for 1.5-ms jitter on each side, setting the lower bound to be 1 ms and the upper bound to be 4 ms. This eliminated peaks that could arise in the 0–1 ms bin due to a shared common input, as well as disynaptic EPSPs that could have latencies longer than ~5 ms (45). Here, for the monosynaptic connectivity inference, we used thalamic spiking as the reference and cortical spiking as the target and examined correlated firing within a lag window of 1–4 ms. The results here were relatively invariant to the specific choice over a range of lag windows, but we found the 1–4 ms window to be the most conservative [i.e., smaller window than 1–5 ms but resulted in same number of pairs classified as “connected”; Supplemental Fig. S3 (see <https://doi.org/10.6084/m9.figshare.14393573.v2>)]. For the spontaneous condition, we segmented the spike train data into 5-s trials (matching duration of stimulus-based trials) and performed cross correlation analysis in a trial-by-trial manner. To measure the level of presynaptic synchronization in thalamus, we performed a cross correlation analysis and computed synchrony strength using a central area under the cross correlogram for all thalamic pairs that responded to the same principal whisker. The principal whisker was identified using the functional responses as measured by the local field potential (LFP) and in the single-unit (SU) data. Thalamic synchrony was computed for each thalamic pair using the total number of spikes within a 15-ms (± 7.5 ms) window of the cross correlogram (N_{cc}), normalized by the mean number of spikes from each neuron (N_{ref} , N_{target}) (14, 20, 26, 40, 46):

$$\text{strength} = \frac{N_{cc}}{\sqrt{\frac{N_{ref}^2 + N_{target}^2}{2}}}$$

Probabilistic measure of connectivity inference.

For each pair of thalamocortical neurons, we repeated the cross-correlational analysis with bootstrapping method. This was done by performing resampling on the data set with replacement, with ~500–1,000 iterations for each condition. By counting the number of iterations that fulfill the criteria for classifying the monosynaptic connection, this resulted in a *P* value that can be attached to the binary classification of monosynaptic connection (see Inferring Connectivity in the Context of a Signal Detection Framework). We refer to this *P* value as the probability of inferring monosynaptic connection, *P*(Inferring “connected”).

Data length effect on the connectivity metric.

Simulation for various data lengths was implemented by using subsamples (in unit of trials) of VPM and S1 spikes for cross correlation analysis. For each data length condition, we computed the resampled peak height, h^* . A bootstrapped estimator of bias was computed as the difference between

the mean of the resampled peak height and the original metric, assuming a normal distribution:

$$\text{bias} = E(h^* - h)$$

where $E(\cdot)$ denotes statistical expectation. The variance was estimated as the square of the resampled peak height:

$$\text{variance} = \text{var}(h^*)$$

A significance level for the inference for a “putatively connected” pair was computed and denoted as the probability of a hit when the peak height metric for the resampled data exceeded the criterion for the inference of a functional connection. The probability of a miss is complementary:

$$P(\text{hit}) = \frac{\#\{h^* \geq \text{criterion}\}}{\#\text{ of iterations}}, \text{ criterion} = 3.5$$

$$P(\text{miss}) = 1 - P(\text{hit})$$

On the other hand, the significance level for a “not-connected” pair was computed and denoted as the probability of a correct reject when the peak height metric for the resampled data is less than the criterion.

$$P(\text{correct reject}) = \frac{\#\{h^* < \text{criterion}\}}{\#\text{ of iterations}}, \text{ criterion} = 3.5$$

$$P(\text{false alarm}) = 1 - P(\text{correct reject})$$

Thalamic synchrony effect on connectivity metric.

Simulation for various thalamic synchrony levels was implemented by manipulating both firing rate and spike timing of VPM and S1. Given that both firing rate and thalamic synchrony were affected with increasing stimulus strength, our simulation was conducted with data that were collected under the spontaneous condition. For a connected pair, we set the ratio between VPM and S1 firing to be constant at each synchrony level for simplification. However, we systematically increased spiking activity (in number of spikes per trial) in VPM and S1 with a specific amount of jitter (zero-mean Gaussian noise of a specific standard deviation, σ) as a function of thalamic synchrony. For a not-connected pair, the increases in thalamic synchrony and VPM and S1 firing were simulated by systematically adding spikes from another pair of neurons that is putatively connected. The assumption here was that a not-connected pair would become more identical to its neighboring neuron (that has a functional connection to the downstream S1 neuron) with increasing synchrony. This was repeated for 100–500 iterations for each synchrony level, and the probability of satisfying *criteria 1* and *2* was computed.

RESULTS

Here, we present a comprehensive experimental and analytic framework for assessing synaptic connectivity using extracellular spiking activity from simultaneously recorded single units across brain structures. First, we provide a rigorous experimental protocol for performing simultaneous single-unit electrophysiological recording in topographically aligned regions in the thalamocortical circuit of the somatosensory pathway using a combination of stereotaxic targeting based on anatomical landmarks, sensory-evoked

response properties, and post hoc histological validation. We highlight some similarities and differences of the technical aspects of paired recordings performed in rats versus mice, two commonly used rodent species in mammalian electrophysiology. Next, we generate inferences regarding the synaptic connectivity of two single units based on spike correlation analysis across the presynaptic VPM and postsynaptic S1 spiking, leading to classification as either connected or not connected, using an approach explained in detail below. Figure 1A highlights the basic experimental setup and analysis utilized in this study, with electrophysiological recordings targeted to primary somatosensory “barrel” cortex (S1; Fig. 1A, red) and to ventro-posteromedial thalamus (VPM; blue), during controlled deflections of a single whisker on the contralateral side of the face with a computer-controlled actuator (see METHODS). In the context of a signal detection framework, we then quantify the effects of experimental data length and local synchrony of presynaptic neurons on monosynaptic connection inference and, importantly, expand this framework to attach statistical levels of confidence to the synaptic connectivity inferences.

Experimental Workflow to Establish Paired Recordings.

Paired recordings in topographically aligned feedforward sensory regions in vivo have been previously shown to be experimentally tractable (12–14, 20, 33), yet it remains a challenging process, and, to our knowledge, detailed reports on experimental approaches have not been published in full. Here, we document the steps in detail. Figure 1B summarizes the general workflow for establishing and analyzing paired recording: 1) mapping primary somatosensory cortex (S1), 2) localizing the ventral posteromedial (VPM) nucleus of the thalamus, 3) achieving and verifying topographical alignment of recording electrodes across VPM and S1, 4) connectivity assessment through statistical analysis of the measured spiking activity from pairs of single units across recording sites, and 5) histological verification of recording site locations.

Although the final electrode placement for paired recording involved thalamic electrode placement followed by placement of the cortical electrode, we found that an initial somatotopic mapping of cortex was critical for efficiently achieving topographical alignment. As part of the approach,

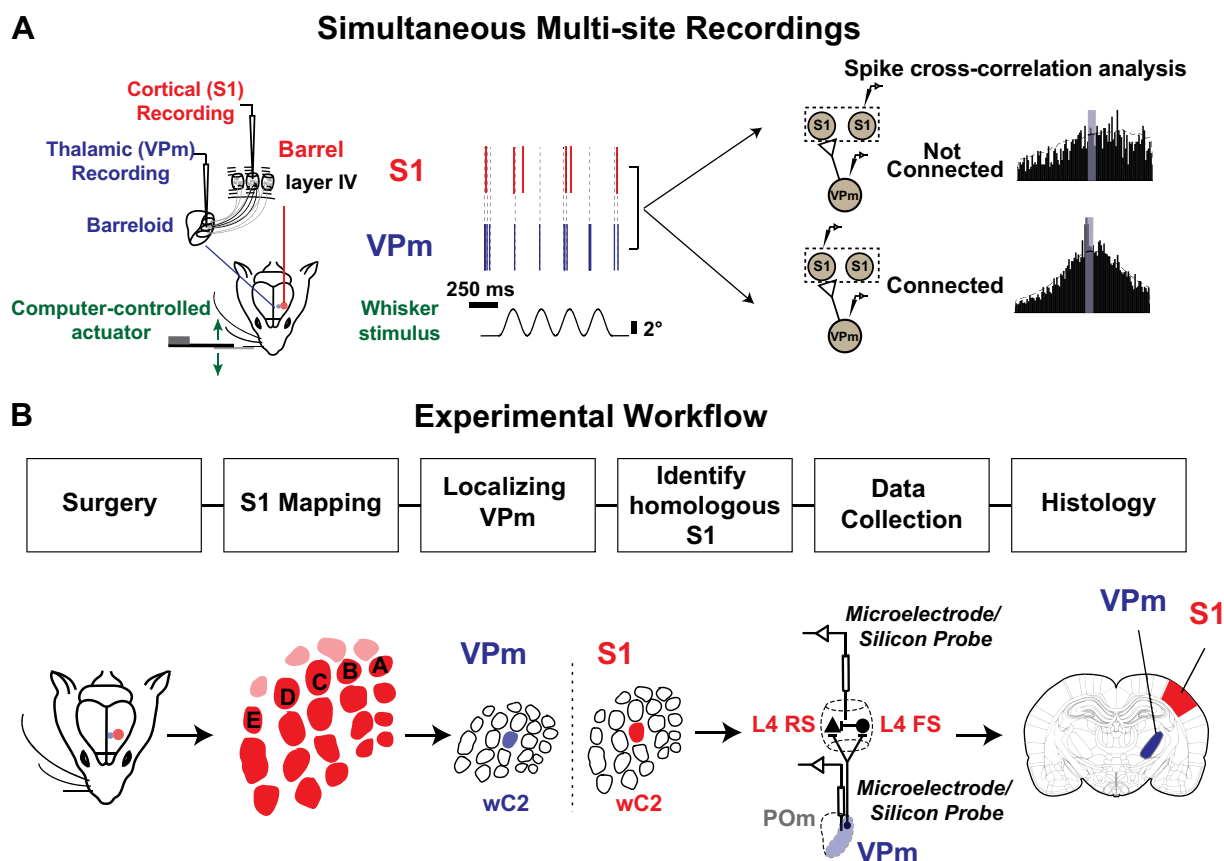


Figure 1. Experimental approach used to estimate monosynaptic connectivity between somatotopically organized areas of the rodent somatosensory pathway. **A:** simultaneous single-unit extracellular recordings were performed in the ventral posteromedial nucleus (VPM) of the thalamus and in layer IV of primary somatosensory cortex (S1) in anesthetized rodents. Recordings were targeted to topographically aligned barreloids in VPM and barrel column in S1. Weak stimulation was applied to the whisker corresponding to the recorded barreloid/barrel column to elicit nonsynchronous spiking. Putative monosynaptic connections between pairs of neurons were inferred with cross correlation analysis. **B:** experimental procedures used to establish paired recordings involve 1) animal preparation including surgeries; 2) S1 mapping; 3) identification of the whisker corresponding to the recorded barreloid; 4) targeting corresponding S1 barrel column and layer IV; 5) data collection for assessing monosynaptic connectivity by generating spikes via whisker stimulation; repeating steps 3, 4, and 5 for recording additional pairs; and 6) histology. FS, fast-spiking unit; L4, layer 4; POm, posteromedial nucleus; RS, regular-spiking unit; wC2, C2 whisker.

we thus first performed coarse cortical mapping before thalamic localization. In rat, we employed primarily electrophysiological mapping approaches for this coarse mapping of S1. We targeted S1 using approximate stereotaxic coordinates and inserted a single electrode to obtain the functional location of several “barrels,” using bregma as a reference point. Once we located the S1 region, we identified the stereotaxic location of three barrel columns containing neurons that were responsive to the movement of single primary whiskers (Supplemental Fig. S1; see <https://doi.org/10.6084/m9.figshare.14393528.v1>). We used this relative distance between columns/barrels to estimate the overall topography of S1 by overlaying a barrel map template scaled to fit the three data points. In mouse, taking advantage of the optical properties of the mouse skull (i.e., that it is relatively translucent), we employed intrinsic optical signal imaging (IOS) for the coarse cortical mapping. Intrinsic optical signals were acquired in response to separate, punctate deflections of three different single vibrissae. The corresponding cortical regions of activation were coregistered with the anatomy of the blood vessels and further used as a landmark for electrode placement. This triangulation methodology was adapted from a previously published method from our laboratory (47, 48). An example of this is shown in Fig. 2A (see also Supplemental Fig. S1A; see <https://doi.org/10.6084/m9.figshare.14393528.v1>). The three images in the top row of Fig. 2A were acquired in response to punctate deflections of the beta whisker (wBeta), the C2 whisker (wC2), and the B2 whisker (wB2), respectively. Each image represents the mean 0- to 6-s poststimulus response (baseline subtracted and scaled) to a 4-s, 10-Hz, 1,000°/s pulsatile stimulus, with the region of cortical activation appearing as a dark spot near the center of the image, at different locations for each whisker. We then fitted a barrel map template, recovered from histological brain sections from previous experiments, onto the overall optical image of the brain surface through the thinned skull (template shown in Fig. 2A, bottom left). The three centroids of the intrinsic imaging signals were used as reference points (Fig. 2A, bottom center) for transformation of the barrel map template involving scaling, rotation, translation, and shearing. This transformed map along with the blood vessel image (Fig. 2A, bottom right) was then used as a navigation guide for electrode placement for targeting a desired barrel column.

Once the cortex was coarsely mapped with the above approaches, we inserted an electrode to localize VPM (see Electrophysiology). Specifically, we identified specific thalamic barreloids by manually deflecting each of the facial vibrissae individually to find an isolated unit that was maximally responsive to a single whisker only. Note that the procedure was nearly identical for rat and mouse, except that for the mouse a silicon multielectrode probe was utilized and localization was performed using one of the probe sites, usually the deepest probe contact. Given that the probe was spanning several hundred micrometers on the thalamic recording site, we typically recorded from one to three barreloids simultaneously with two or more recording sites within a single barreloid. Final placement of the electrode was fixed when well-isolated units were detected on probe contacts. For verification of barreloid targeting within VPM, we

compared local field potential (LFP) responses to individual stimulation of multiple nearby vibrissae. Figure 2B shows an example of LFPs recorded in the A3 barreloid of thalamus on one of the probe contacts. Note that the evoked LFP response exhibits an initial negative peak for the whisker A3 deflection (Fig. 2B, wA3, blue) that is substantially larger than responses to the deflection of other whiskers.

A practical challenge lies in the positioning of the recording electrodes to reach the multiple target areas. In a small subset of experiments, we optimized the electrode insertion angle by coating the electrodes with fluorescent dye (DiI) to mark the electrode track for postexperiment histological analysis. A range of insertion angles was tested for both S1 and VPM in mouse and rat. We found that the optimal electrode angle to target VPM thalamus in both rats and mice was 0° from vertical (perpendicular to the brain surface) (Fig. 2C, left, and Supplemental Fig. S1B; see <https://doi.org/10.6084/m9.figshare.14393528.v1>). For S1 targeting, we found that the optimal angle was ~40–45° from vertical for rats and was ~30–35° from vertical for mice for electrode penetration parallel to the cortical column/barrel, important for accurate targeting of specific cortical depths. The target recording site depths were determined based on published anatomical locations of the target structures (see METHODS). Figure 2C shows typical electrode tracks targeting S1 and VPM in a mouse (Fig. 2C, left), along with the corresponding raw extracellular recordings from one VPM and one S1 electrode recording site (Fig. 2C, center). Both the VPM and S1 extracellular recordings show sensory-driven responses to deflections of the same whisker, the pattern of which is shown in the extracellular recordings of Fig. 2C; the times of whisker stimulation are denoted with green arrows, representing a pattern of two isolated whisker deflections, followed by an 8-Hz train of whisker deflections. The raw electrophysiological recordings were subsequently sorted into single-unit data based on conventional spike sorting approaches, and only well-isolated units were retained for analysis (see METHODS). For each recording, the identified putative single-unit spiking (red and blue in Fig. 2C) is superimposed on the raw recording (light gray), and the corresponding spike times are denoted above each trace (red and blue triangles). For each case, the spike waveform and spike autocorrelogram are shown in Fig. 2C, right. A summary of the waveform size and isolation quality for all recorded VPM and S1 units is shown in Supplemental Fig. S1C; see <https://doi.org/10.6084/m9.figshare.14393528.v1>.

Sensory Response in Topographically Aligned VPM–S1 Layer 4 Regions

Achieving topographically aligned recordings across corresponding thalamic barreloids and cortical barrel columns necessitates the accurate targeting of the thalamic recording electrode/probe to the VPM nucleus of the thalamus. In particular, it is key to be able to distinguish whisker-responsive units located in VPM from those located in the adjacent posteromedial nucleus (POM) of the thalamus. In previous studies, POM units have been shown to exhibit lower evoked firing rate (25, 49–51) and much broader receptive fields than VPM units, responding to ~6 vibrissae on average, ranging from 3 to 12 whiskers (49, 52). Hence, to ensure recordings

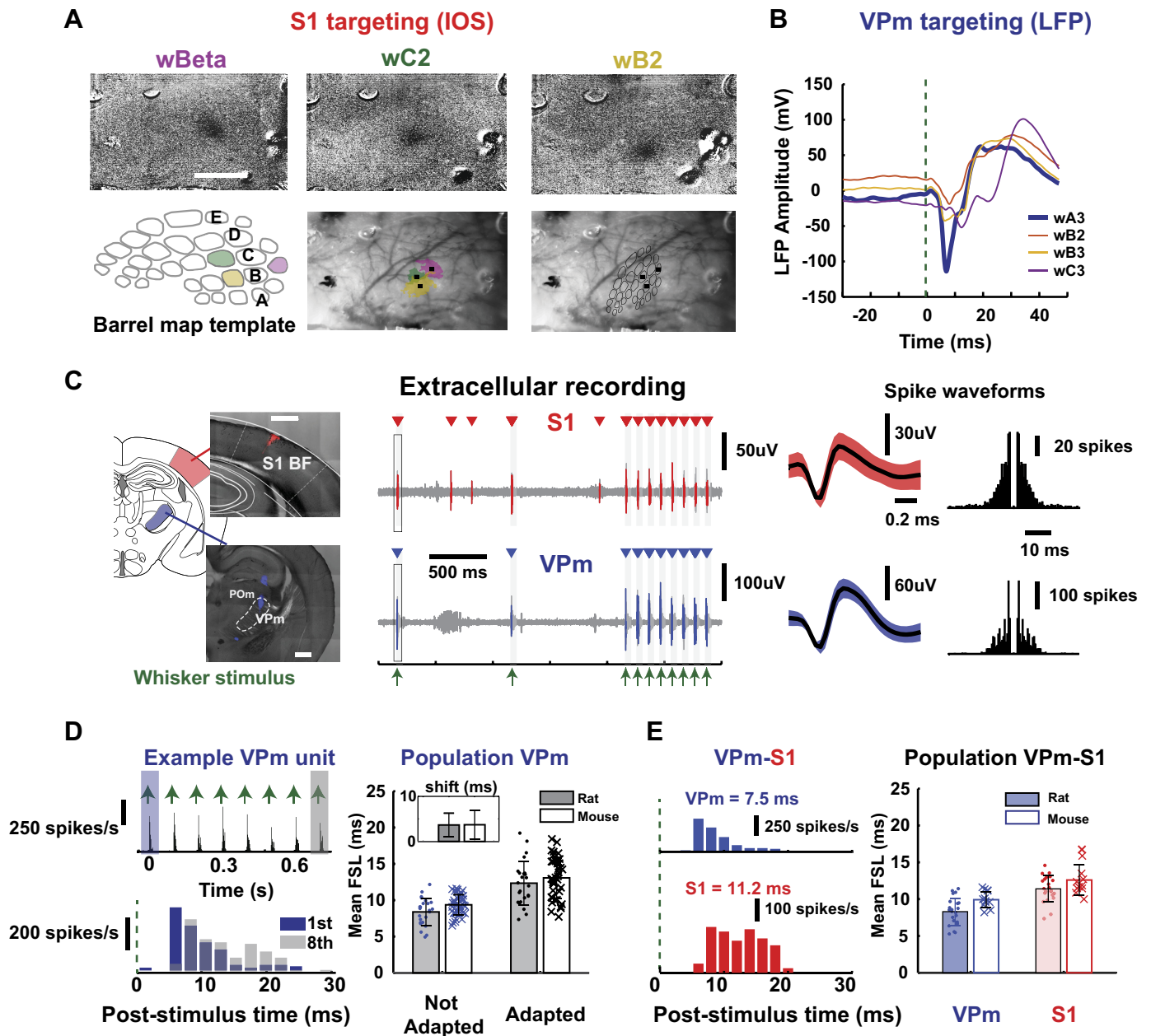


Figure 2. Targeting topographical alignment in vivo. *A*: primary somatosensory cortex (S1) targeting: Location of S1 barrels was determined with intrinsic imaging (IOS) in mice. The 3 images at *top* are images acquired in response to separate single punctate deflections of the beta whisker (wBeta), the C2 whisker (wC2), and the B2 whisker (wB2). A barrel template was compared with the optical image of the brain surface through the thinned skull and fitted based on the location of the centroid of barrels to provide guidance for electrode placement. *B*: ventral posteromedial nucleus (VPM) targeting: example mean local field potential (LFP) amplitude of evoked response (shown by downward deflection after stimulus onset) for 4 stimulated whiskers in mice. Note the largest and fastest response to the A3 vibrissa and the comparatively weak responses to the adjacent B2, B3, and C3 vibrissae, lending support for VPM localization. *C*, *left*: histological slice showed electrode tracks marked with fluorescent dyes (see Postmortem Histology) on coronal brain sections targeting VPM (*bottom*) and S1 layer IV (*top*) in a mouse. *Center*: example raw voltage traces from extracellular recordings performed simultaneously in VPM and S1 layer IV during sensory stimulation in a rat. Mean waveforms of isolated single units from each recording site are shown (shaded region indicates 1 standard deviation of spike amplitude) *Right*: spike autocorrelograms of each unit in a rat. *D*, *left*: example adapting response of a single thalamic unit from a rat, showing mean first spike latency in response to first and last pulses of a 8-Hz pulsatile, ongoing stimulus (first pulse: 5.18 ms, last pulse: 10.7 ms). *Right*: population adapting response for thalamic units recorded in rats and mice [first pulse (rats): 8.39 ± 1.87 ms, last pulse (rats): 12.3 ± 3.04 ms, $n = 24$ neurons, $N = 12$ rats; first pulse (mice): 9.37 ± 1.39 ms, last pulse (mice): 13.1 ± 2.78 ms, $n = 39$ neurons, $N = 4$ mice]. *Inset*: all thalamic units that we recorded showed latency shift < 20 ms [latency shift (rats) = 3.65 ± 2.62 ms, $n = 24$ neurons, $N = 12$ rats; latency shift (mice) = 3.71 ± 3.11 ms, $n = 39$ neurons, $N = 4$ mice], suggesting that they were thalamic VPM units. *E*, *left*: example peristimulus time histogram (PSTH, 2-ms bin size) for a thalamic and a cortical unit in the 30-ms window following punctate ($600^\circ/\text{s}$) whisker stimulus (indicated by green dashed line at $t = 0$). We computed mean first spike latency (FSL), defined as average latency of first spike in 30-ms response windows after stimulus presentation for each unit (VPM: 7.5 ms, S1: 11.2 ms). *Right*: population mean FSL for all simultaneously recorded thalamic and cortical units in rats and mice [VPM (rats): 8.30 ± 1.84 ms, S1 (rats): 11.40 ± 1.77 ms, $n = 22$ neurons, $N = 12$ rats; VPM (mice): 9.80 ± 1.31 ms, $n = 9$ neuron; S1 (mice): 12.6 ± 2.06 ms, $n = 11$ neurons, $N = 1$ mouse]. BF, barrel field.

from primarily VPM neurons, we selected thalamic units that showed restricted whisker sensitivity, usually only to one principal whisker (as shown in Fig. 2B). The thalamic single units kept for subsequent connectivity analysis exhibited strong, reliable response (response reliability: $52.6 \pm 24.62\%$; not shown) to a punctate whisker stimulus with short latency [first pulse (rats): 8.39 ± 1.87 ms (mean \pm SE), last pulse (rats): 12.3 ± 3.04 ms (mean \pm SE), $n = 24$ neurons, $N = 12$ rats; first pulse (mice): 9.37 ± 1.39 ms (mean \pm SE), last pulse (mice): 13.1 ± 2.78 ms (mean \pm SE), $n = 39$ neurons, $N = 4$ mice; Fig. 2, D and E; Supplemental Fig. S2A; see <https://doi.org/10.6084/m9.figshare.14393570.v1>]. As an additional criterion, we measured the adapting properties of the thalamic units in response to repetitive, periodic whisker stimuli (25, 38, 53). Previous studies have shown that neurons in POM exhibit dramatic adaptation to persistent sensory stimulation, where most POM neurons failed to exhibit a response to stimuli ≥ 11 Hz (38), and a significant shift in response latency with the adaptation, compared with VPM neurons (25, 51). Here, we showed a representative thalamic unit spiking response to an 8-Hz adapting whisker stimulus in Fig. 2D, left, with a PSTH in response to the full stimulus train (top) and a superposition of the stimulus evoked response to the 1st (blue) and 8th (gray) deflections in the train (bottom). This particular example shows strong stimulus-locked responses and moderate adaptation (i.e., reduction in response amplitude), with a relatively small increase in latency of spiking. In fact, all the thalamic units that we considered for further analysis showed only moderate spike frequency adaptation, with a maximal increase in latency of 8 ms when comparing responses to the first and last stimulus of the train [mean first spike latency (FSL), latency shift from not adapted to adapted = 4.28 ± 2.32 ms (mean \pm SE), $n = 21$ cells from rat; 3.71 ± 3.11 ms (mean \pm SE), $n = 39$ neurons, $N = 4$ mice; Fig. 2D, right, inset]. Furthermore, the response latency of thalamic neurons measured here is consistent with the latency of VPM neurons (peak latency < 10 ms) identified through a genetic validation approach (54). Note that there remains a small possibility that a subset of the thalamic units are POM in origin and project to S1 interbarrel areas (septa). However, this is unlikely to be the case for the thalamo-cortical pairs that showed monosynaptic connectivity, given that these thalamic and cortical units demonstrated mostly single whisker receptive fields (55) and the likelihood of detecting synaptic connections in POM-S1 interbarrel areas is much lower. Finally, a recent study showed that POM cells remain largely inactive (close to zero spontaneous firing rate) under isoflurane anesthesia (56), making them extremely difficult to locate and record from under the conditions of this study, which when combined with the other factors described above makes it unlikely that any of the recordings here are POM in origin. Again, note that the challenges here are somewhat specific to this particular brain region, but achieving definitive recordings in other brain regions would likely have challenges similar to those described here.

Previous studies have shown that the convergence of thalamic inputs onto topographically aligned cortical layer IV neurons is generally relatively high, but with the probability of contacting regular spiking units (RSUs) much lower than fast-spiking units (FSUs) (33, 44). We recorded from well-

isolated cortical layer IV neurons (see Supplemental Fig. S1C) at a cortical depth taken from micromanipulator readings (rat: 803.28 ± 175.28 μm , mean \pm SE, $n = 21$, data not shown; mouse: $350\text{--}700$ μm , $n = 11$, see Fig. 5B). All cortical units included in this study were putatively layer IV neurons. The mean first spike latency of cortical units was 11.4 ± 1.77 ms (mean \pm SE, $n = 22$) for rat and 12.6 ± 2.06 ms (mean \pm SE, $n = 11$) for mouse. We found that the relative latency difference between VPM and S1 layer IV in aligned regions was comparable to the expected synaptic delay between VPM and S1 layer IV (differences between VPM and S1 were ~ 3 ms for both rat and mouse). An example of the response to a punctate whisker stimulus for a pair of VPM and S1 FS units with mean first spike latency of 7.5 ms and 11.2 ms is shown in Fig. 2E, left.

Inferring Connectivity in the Context of a Signal Detection Framework

In general, neurons in the central nervous system require the concerted action of a relatively large number of presynaptic inputs to produce an action potential (20). Thus, the relationship between pre- and postsynaptic neurons is tenuous at best, reflected in often a very subtle increase in the probability of firing of the postsynaptic neuron a few milliseconds after the firing of a presynaptic neuron. The analysis of spike trains from a pair of neurons can thus be utilized for a simple binary classification of a neuronal pair being either not connected or connected (Fig. 3A). To infer connectivity, for each recorded pair of neurons, the raw spike cross correlogram is calculated with standard approaches (C_R , Fig. 3C) (see METHODS), effectively yielding a histogram of cortical firing relative to thalamic spike times. Because the analysis is based on spiking activity, and the baseline spiking activity can often be relatively low, we drove the thalamo-cortical circuit in vivo with a weak whisker stimulus (Fig. 3B; sinusoidal deflection: 4 Hz, mean velocity: $25^\circ/\text{s}$), which is known to enhance firing rates with minimal impact on firing synchrony across neurons (20). To correct for correlated stimulus-locked activity, we generated a shuffled-corrected spike cross correlogram (C_{SC} ; Fig. 3E) by subtracting the trial shuffled spike cross correlogram (C_S ; Fig. 3D) from the raw spike cross correlogram. The “shuffled cross correlogram” is generated with the same procedure used for the raw cross correlogram, except that the trials of the thalamic and cortical spiking activity are randomized relative to each other. This effectively destroys any elements of the cross correlogram that are not due to the stimulus. Shown in this example is the qualitative signature of monosynaptic connectivity—a prominent peak in the shuffled-corrected cross correlogram for small positive lags that would be consistent with a single synaptic delay.

Then, to conclude that a neuronal pair was connected, we adopted two criteria that expanded from previous studies (12, 13, 20) based on both the raw and shuffled-corrected cross correlogram: a notable sharp, millisecond-fine peak is observed within a narrow lag of 1–4 ms after a thalamic spike (criterion 1), and this fast “monosynaptic peak” is significant or still present after accounting for (subtracting) stimulus-

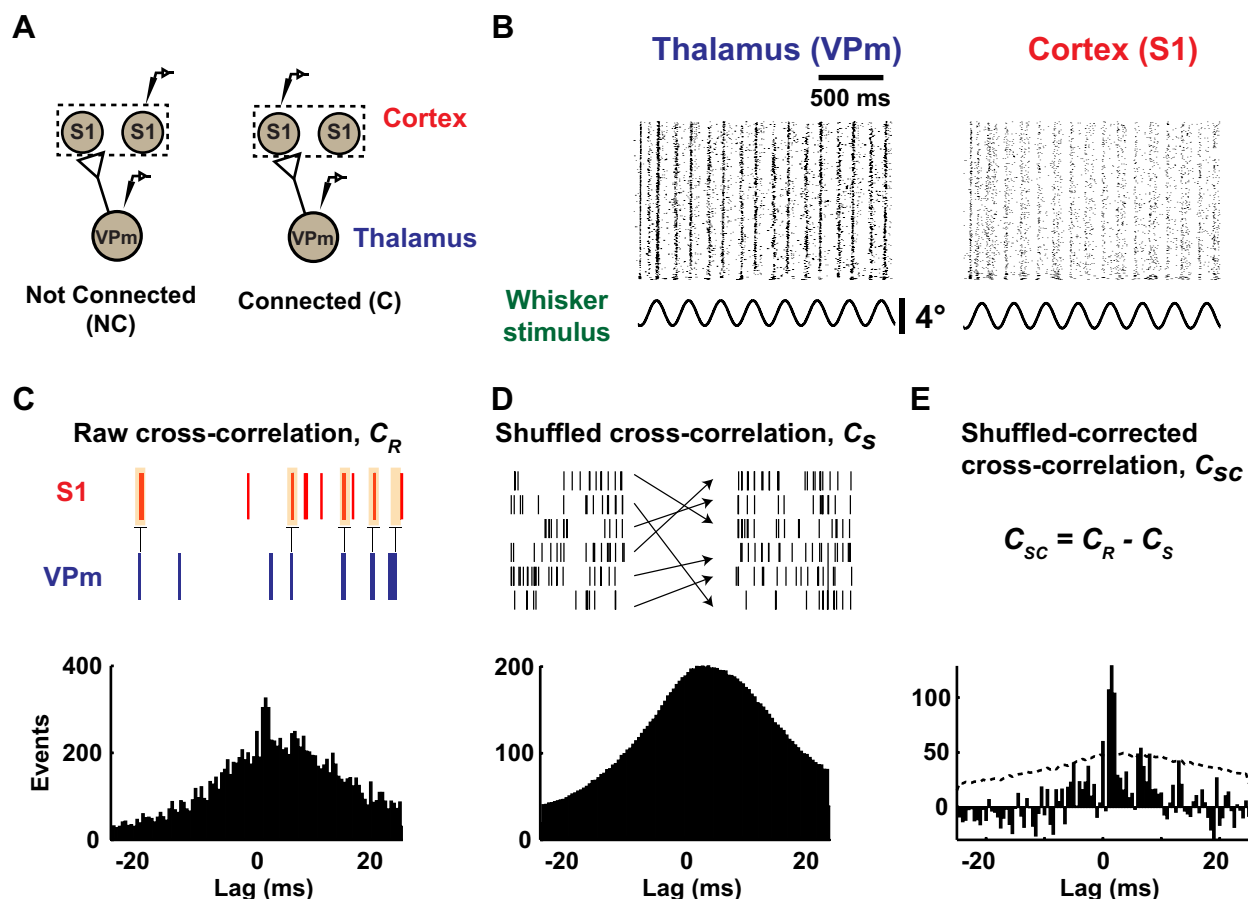


Figure 3. Monosynaptic connectivity inference using cross correlation analysis. **A:** inferring monosynaptic connectivity from extracellular recordings performed in topographically aligned thalamocortical regions in vivo resulted in binary consequences. A pair of neurons can be putatively classified as connected or not connected, as shown in the schematic. S1, primary somatosensory cortex; VPm, ventral posteromedial nucleus. **B:** raster plots showing whisker-evoked spiking response under low-velocity sinusoidal stimulation (mean velocity: 25°/s) for a representative example from thalamus and cortex in a rat. **C:** all cross correlograms were computed using VPm spike train as a reference. Occurrences of cortical spikes were measured at various time lags (25-ms window before and after a thalamic spike, with 0.5-ms step size; see METHODS). **D:** stimulus-driven cross correlograms were constructed between the original reference VPm spike trains and the trial-shuffled cortical spike trains. **E:** shuffled-corrected cross correlograms were generated by subtracting the mean of shuffled cross correlograms (averaged from 1,000 iterations) from the raw cross correlograms. Dotted gray lines denote 3.5 standard deviation of the shuffled distribution.

induced correlation (*criterion 2*). Note that a peak is defined as the bin in the raw cross correlogram (0.5-ms bin size) that contains the maximum number of events. To fulfill both criteria, we required the peak detected in the 1–4 ms range to have the largest correlation out of all the bins in the range of ± 25 ms window and this correlation to be significant (>3.5 SD) against shuffled data. For the example connected pair in Fig. 3, C–E, and a separate not-connected pair, *criterion 1* is evaluated from the raw cross correlation as shown in Fig. 4A. For the not-connected example (raw cross correlogram, Fig. 4A, left), a peak was detected outside the central 1–4 ms lag and thus fails *criterion 1*. The example connected pair, and the raw cross correlogram in Fig. 4A, right, exhibits a peak within the central 1–4 ms lag (shown as a vertical gray band) and thus passes *criterion 1*. Figure 4A illustrates how *criterion 2* is estimated from the shuffled-corrected cross correlation. We evaluate the prominence of the peak relative to a distribution of peak magnitudes (same bin with maximum number of events) from the shuffled cross correlograms (1,000 iterations).

Specifically, we define the metric related to *criterion 2* as the peak height, h , computed using the maximum of the C_{SC} (0.5-ms bin size) within 1–4 ms lags, normalized by the standard deviation of the shuffled cross correlogram. This metric is thus the number of standard deviations the peak of the shuffled-corrected cross correlogram within the 1–4 ms lag is above the shuffled distribution. This is shown in more detail for this example in the insets in Fig. 4A, bottom, where the central portions of the shuffled-corrected cross correlograms are shown for each case. To pass *criterion 2*, the peak height of the shuffled-corrected cross correlograms must be >3.5 standard deviations of the shuffled data, which corresponds to a 99.9% confidence interval for each bin.

Thus, we conclude that the shuffled-corrected cross correlograms on the left in Fig. 4A fail *criterion 2*, as the peak falls below the criterion line (3.5 SD, depicted as dashed line), whereas the shuffled-corrected cross correlograms on the right pass *criterion 2*. Note that for the not-connected pair shown in Fig. 4A, the shuffled-corrected cross correlogram

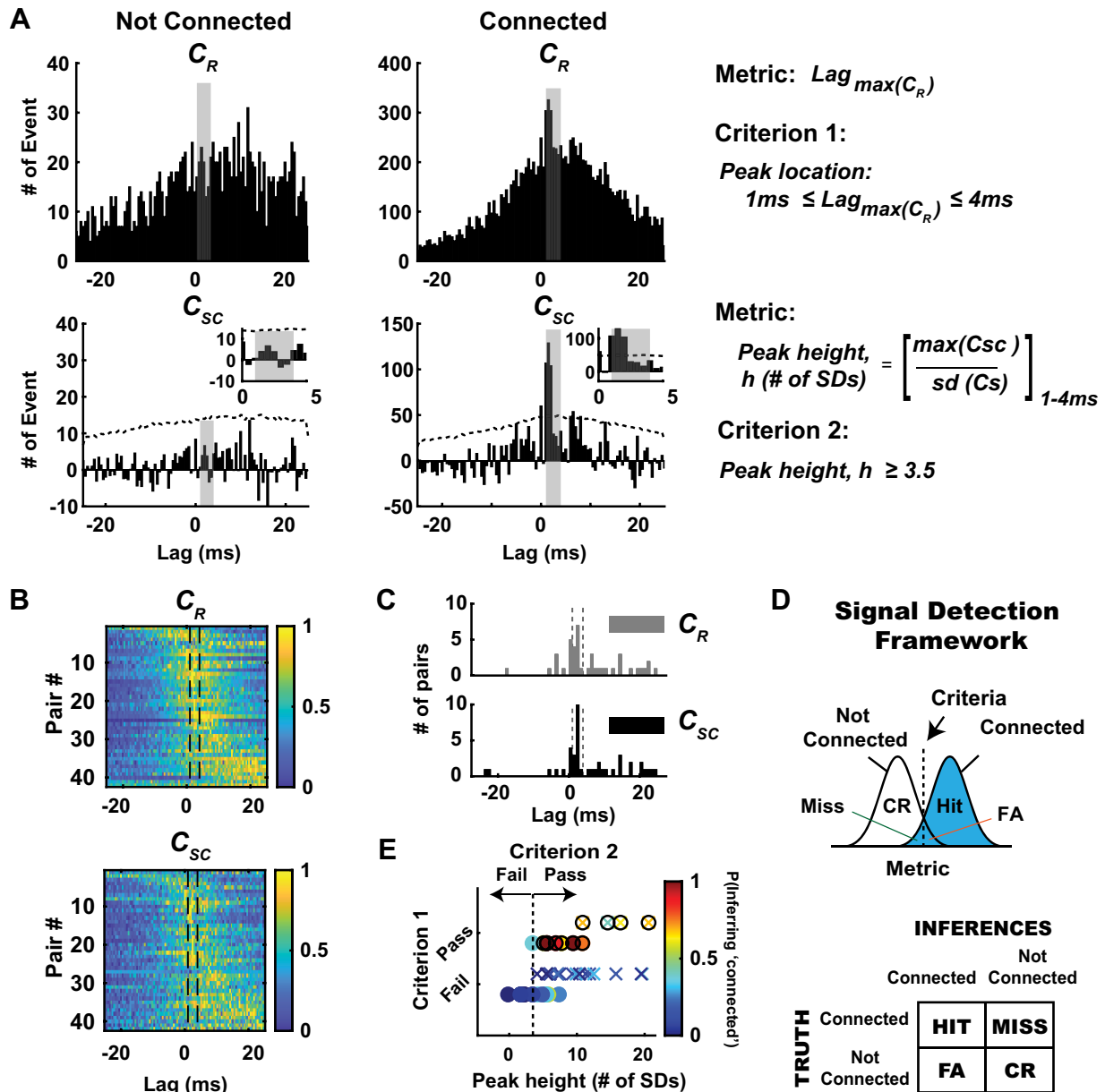


Figure 4. Evaluation of monosynaptic connection inference in the context of a signal detection framework. **A:** in the context of signal detection framework, we defined 2 distinct metrics and criteria to classify neuronal pairs into connected and not-connected distribution. Shown here are representative example pairs from each condition. *Top:* note the qualitative difference in raw cross correlograms (C_R), one with broad and distributed spikes in cross correlogram (*left*) and another with sharp peaks (*right*) in 1–4 ms time lags (shaded gray). The first metric is the maximum peak of the raw cross correlogram (C_R), and *criterion 1* was fulfilled if the maximum peak of the raw cross correlograms was within 1–4 ms lag. *Bottom:* after correcting for stimulus-driven correlations, we further quantified the significance of the peaks detected in raw cross correlogram. Hence, the second metric used here is the peak height within the window of interest (1–4 ms bin), measured as maximum peak value in shuffled-corrected cross correlogram (C_{SC}), normalized to the number of standard deviations (SDs) with respect to the shuffled distribution. *Criterion 2* was fulfilled if the peak exceeded 3.5 SDs of the shuffled distribution. **B:** as expected, the majority of simultaneously recorded thalamocortical pairs exhibited peak correlation after 0 time lag ($n = 42$ pairs; rats: 22, mice: 20). Histograms show the number of events in each bin of raw cross correlograms (*top*) and shuffled-corrected cross correlograms (*bottom*), sorted by latency of maximum peak in the cross correlograms. Data were normalized to maximum peak, and the colors in each row show the number of events for an individual pair, normalized to maximum peak. **C:** distribution of the lags of the peak location in the raw and shuffled-corrected correlograms across all recorded pairs. Note that the peak locations for raw and shuffled-corrected correlograms were largely the same, shifted only by 1–2 bin size (0.5-ms bin). **D:** within this framework, 4 possible outcomes are possible: hit: connected and inferred to be connected; miss: connected but inferred to be not connected; false alarm (FA): not connected but inferred to be connected; correct rejection (CR): not connected and inferred to be not connected. **E:** in this context, we found that 11/42 pairs have putative monosynaptic connection (denoted by filled circles) and 31/42 pairs. Pairs were not connected ($n = 22$ pairs, $N = 12$ rats; $n = 20$ pairs, $N = 1$ mouse). Note that *criterion 1* was a binary classification: pairs having peak locations from their raw cross correlograms within the 1–4 ms lag pass *criterion 1*, and those that do not fail *criterion 1*. For *criterion 2*, the dashed vertical line represents 3.5 SDs for the peak height metric: pairs having peak height above this criterion line pass *criterion 2*. Only pairs that passed both *criteria 1* and *2* were classified as connected [anything to the right of the vertical dashed line in *E* (*top row*)], and the rest were classified as not connected. For each recorded pair, probability of inferring monosynaptic connection (i.e., probability of bootstrapped data satisfying *criteria 1* and *2*) is depicted with a color bar. Note that 1,000 iterations were performed for each data set.

also revealed the presence of the global peak outside the 1–4 ms central lag, similar to that of the raw cross correlogram. Thus, it is possible to utilize the shuffled-corrected cross correlogram for the evaluation of *criterion 1* in some cases, but overall we found that *criterion 1* was more robustly evaluated by utilizing the raw cross correlogram. The raw and shuffled-corrected correlograms for all recorded thalamocortical pairs are shown in Fig. 4B, normalized to the peak in each correlogram, ordered from earliest to latest peak, top to bottom. The vertical lines in these plots highlight the 1–4 ms lag range described in Fig. 4. Figure 4C shows the distribution of the lags of the peak location in the raw and shuffled-corrected correlograms across all recorded pairs. Overall, the peak locations for raw and shuffled-corrected correlograms were similar, shifted only by 1–2 bin size (0.5 ms). For all the monosynaptically connected pairs in this report, the mean peak location was 1.18 ± 1.08 ms (mean \pm SE, $n = 11$), with a median of 1.5 ± 0.89 ms.

Note that to be classified as connected, a candidate pair of neurons must pass both *criterion 1* and *criterion 2*. Using these metrics and criteria, we can consider the result of cross correlation analysis for each pair as an inference problem in the context of a signal detection framework, where we conceptualize the distribution of metric values for the nonconnected pairs as “noise” and for the connected pairs as “signal.” Applying the criteria on the metric values yields four possible outcomes: Hit (connected pair classified/inferred as such), Miss (connected pair classified/inferred as not connected), False Alarm (not-connected pair classified/inferred as connected), and Correct Reject (not-connected pair classified/inferred as such) (Fig. 4D). With these metrics and criteria, we classified measured neuronal pairs into connected and not-connected distributions, with 11/42 pairs having a putative monosynaptic connection and 31/42 pairs having no apparent connection (Fig. 4D, bottom; rat: $n = 22$ pairs, mouse: $n = 20$ pairs). For *criterion 1*, this was a binary classification because of biological constraints (single synaptic delay): pairs having peak locations from their raw cross correlograms within the 1–4 ms lag pass *criterion 1*, and those that do not fail *criterion 1*. For *criterion 2*, the dashed vertical line in Fig. 4D, top, represents the 3.5 SD for the peak height metric: pairs having peak height above this criterion line pass *criterion 2*. Only pairs that passed both *criterion 1* and *2* in Fig. 4D, bottom, were classified as connected (anything to the right of vertical dashed line and on the top row), and the rest were classified as not connected. Note that although this is a binary classification, and the end result is a labeling of a pair as connected or not connected, not all classifications are equivalent, with some having substantially more confidence in the classification than others. By utilizing a bootstrapping approach (see METHODS) and evaluating the likelihood of specific outcomes using the predefined metrics and criteria for each recorded pair, we were able to attach a probability measure [Fig. 4E, color bar, $P(\text{Inferring “connected”})$] along with each connectivity inference. In Fig. 4E, some of the cases that passed *criterion 1* have peak heights that are substantially far away from the line for *criterion 2*. As expected, the likelihood of inferring monosynaptic connection for these cases was higher (~ 0.6 – 1), and thus we

have more confidence in the assertion compared with cases that are very close to the criterion line for *criterion 2* or failed *criterion 1*.

Probabilistic Measure of Connectivity Inference across Brain Structures in Large-Scale Recordings

Through the advent of high-channel-count electrophysiological recording techniques (6, 9, 57), the diversity of recording quality, cell type, and possibilities for connectivity has expanded tremendously. To demonstrate how our framework can be beneficial, Fig. 5 shows an example of simultaneous topographically aligned recordings from silicon multielectrode probes inserted in VPM thalamus (Fig. 5A) and S1 (Fig. 5B). Specifically, focusing on portions of the probes that were assessed to be topographically aligned, a subset of channels from the VPM probe (channels A–D) yielded five thalamic neurons (VPM 1–5), whereas a subset of channels from the S1 probe (A–D) yielded four cortical neurons (S1 1–4). These neurons were recorded during weak sinusoidal (25°/s, 4 Hz) whisker stimulation. In this multidimensional analysis, each of the 20 thalamocortical pairs was assessed for the possibility of connectivity. Figure 5C, Table 1, shows the matrix of binary outcomes of monosynaptic connectivity inference from cross correlation analysis of the full data set across the recording sites. Of the 20 VPM–S1 pairs, 4 were judged to be connected according to our criteria. Note that although the connectivity from an individual barreloid to the homologous cortical barrel is relatively high [it has been estimated that ~ 1 in 3 VPM neurons within a barreloid is connected to a particular neuron in cortical layer 4 of the homologous barrel (20)], the relatively stringent criteria of the inference coupled with other factors such as the potential to record from multiple nearby VPM barreloids and variable single-unit quality make this outcome typical. Shown in Fig. 5C, Table 2, are the probabilities of connectivity associated with each pair by using the bootstrapping method ($n = 1,000$ iterations) on the data, as previously described. In general, the binary inference for a particular pair corresponded to the bootstrapped confidence levels: connected pairs had a relatively high probability of connectivity from the bootstrapping (see all connected pairs in Supplemental Fig. S4; see <https://doi.org/10.6084/m9.figshare.14393579.v2>), whereas not-connected pairs had a relatively low probability of connectivity from the bootstrapping ($P < 0.4$). We found that the binary outcomes of monosynaptic connectivity inference could result in different ranges of probability of inferring monosynaptic connection (0.4–1). One factor that could affect this probability is data length. Not surprisingly, we found that the connected pair that yielded the lowest probability in this matrix ($P = 0.41$) had $\sim 3,900$ spikes (in terms of geometric mean) compared with the others (4,900, 6,900, and 10,000 spikes).

Data Length Effect on Monosynaptic Connection Inference

As previously shown, inference of monosynaptic connectivity using cross correlation analysis on extracellular signals is highly dependent on the amount of collected data. Based on existing literature, the recommended numbers of spikes

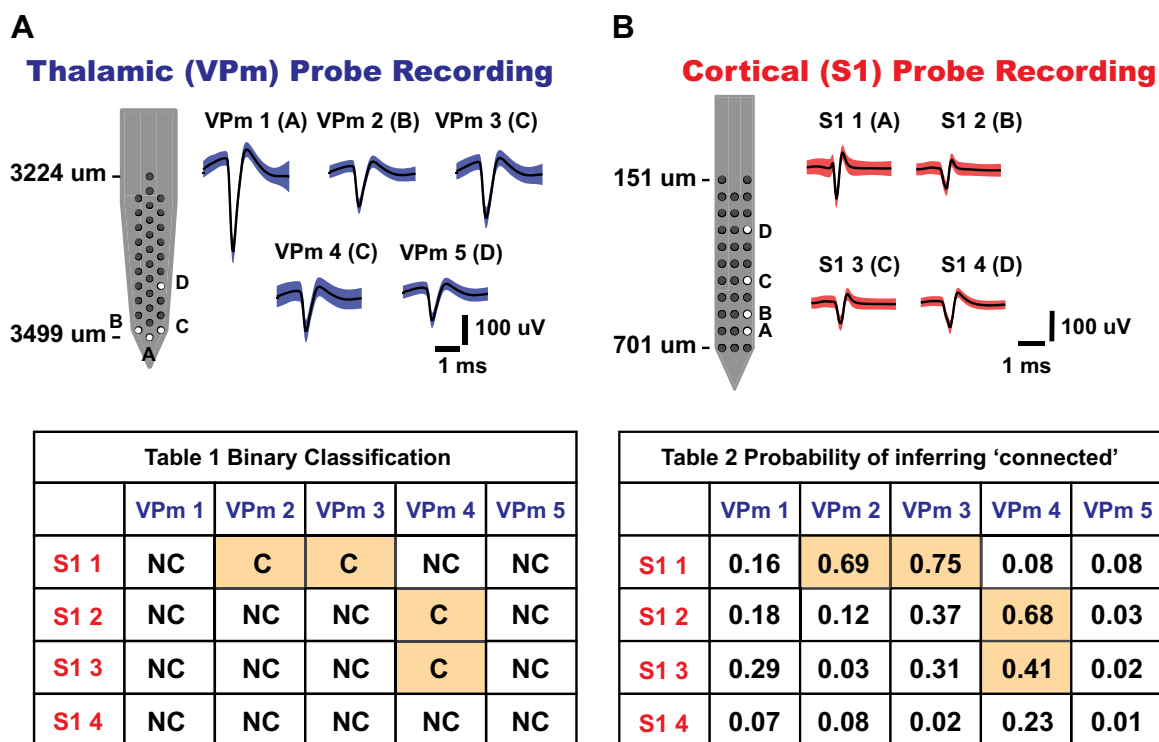


Figure 5. Connectivity matrix for topographically aligned, simultaneous multisite recordings. *A*: thalamic[ventral posteromedial nucleus (VPm)] probe recording. Five whisker-responsive thalamic units were isolated from 32-channel silicon probe sites, labeled *A–D*. Mean waveforms of single units are shown on *right* (shaded region indicates 1 standard deviation of spike amplitude) ($n = 5$ neurons). *B*: cortical [primary somatosensory cortex (S1)] probe recording. Four whisker-responsive units, putatively from layer IV barrel cortex, were isolated from 32-channel silicon probe sites, labeled *A–D*. Mean waveforms of units are shown on *right* (shaded region indicates 1 standard deviation of spike amplitude) ($n = 4$ neurons). Table 1 shows binary outcomes of the monosynaptic connectivity inference based on *criteria 1* and 2 of cross correlation analysis. Table 2 shows the connectivity matrix tabulating the probability of inferring a putative monosynaptic connection using the bootstrapping method for each thalamocortical pair in Table 1 (bootstrap iteration = 1,000). C, connected; NC, not connected.

were highly variable, ranging from 2,000 to 10,000 spikes (13, 14), but were presented more as a “rule of thumb” than based on systematic evaluation. Here, we systematically evaluated data length dependence effects on the connectivity inference outcomes. More specifically, we measured the data length effect by performing bootstrapping on the full data set by randomly selecting segments of data of increasing duration, as illustrated in Fig. 6A. Note that for this analysis the effects of data length were evaluated in the context of *criterion 2*, as this is the measure more prominently affected by data length. In general, the analysis is primarily sensitive to the number of spikes used in the estimates, rather than the time duration of experimental data collection, and is sensitive to the number of both VPm and S1 spikes (i.e., sufficient spiking from both is requisite). For this reason, we utilized the geometric mean of the number of VPm and S1 spikes, calculated as the square root of the product of the number of VPm and S1 spikes. Because we did not have access to an established ground truth of a pair being either connected or not connected, we utilized example pairs in which the analysis revealed a very clear classification, which we subsequently utilized as ground truth for the analysis.

Figure 6 shows the results from such an analysis for a not-connected pair (Fig. 6, *B–E*) and a connected pair (Fig. 6, *F–I*). We found that when a functional connection was

obviously not present, the correlated firing activity between a pair of neurons was indistinguishable from that expected from stimulus-induced correlation, reflected in the metric remaining well below the criterion line (3.5 SD) for all values of data length but, however, steadily increasing as a function of the geometric mean (also accompanied by a decrease in the variability of the metric as reflected in the SE) (Fig. 6C). Figure 6D shows the distributions of the estimated connectivity metric h for two particular data lengths (geometric means of 1,837 spikes and 4,730 spikes), relative to the criterion line. Both of these distributions are clearly to the left of the criterion line, corresponding to high correct reject and low false alarm rates, relatively unaffected by data length (Fig. 6E).

In contrast, when a functional connection was apparent, limited data confounded the inference of “connected,” as the metric remained below the criterion line for smaller data lengths (Fig. 6G). For two particular data lengths (geometric means of 3,760 and 10,201 spikes), the distributions of the estimated connectivity metric h are shown in Fig. 6H relative to the criterion line. Whereas the longer data length resulted in a distribution of the peak height that was clearly above the criterion line (easily passing *criterion 2*), the shorter data length resulted in a distribution whose mean was above the criterion line (barely passing *criterion 2*) but with a substantial portion of the distribution below the criterion line,

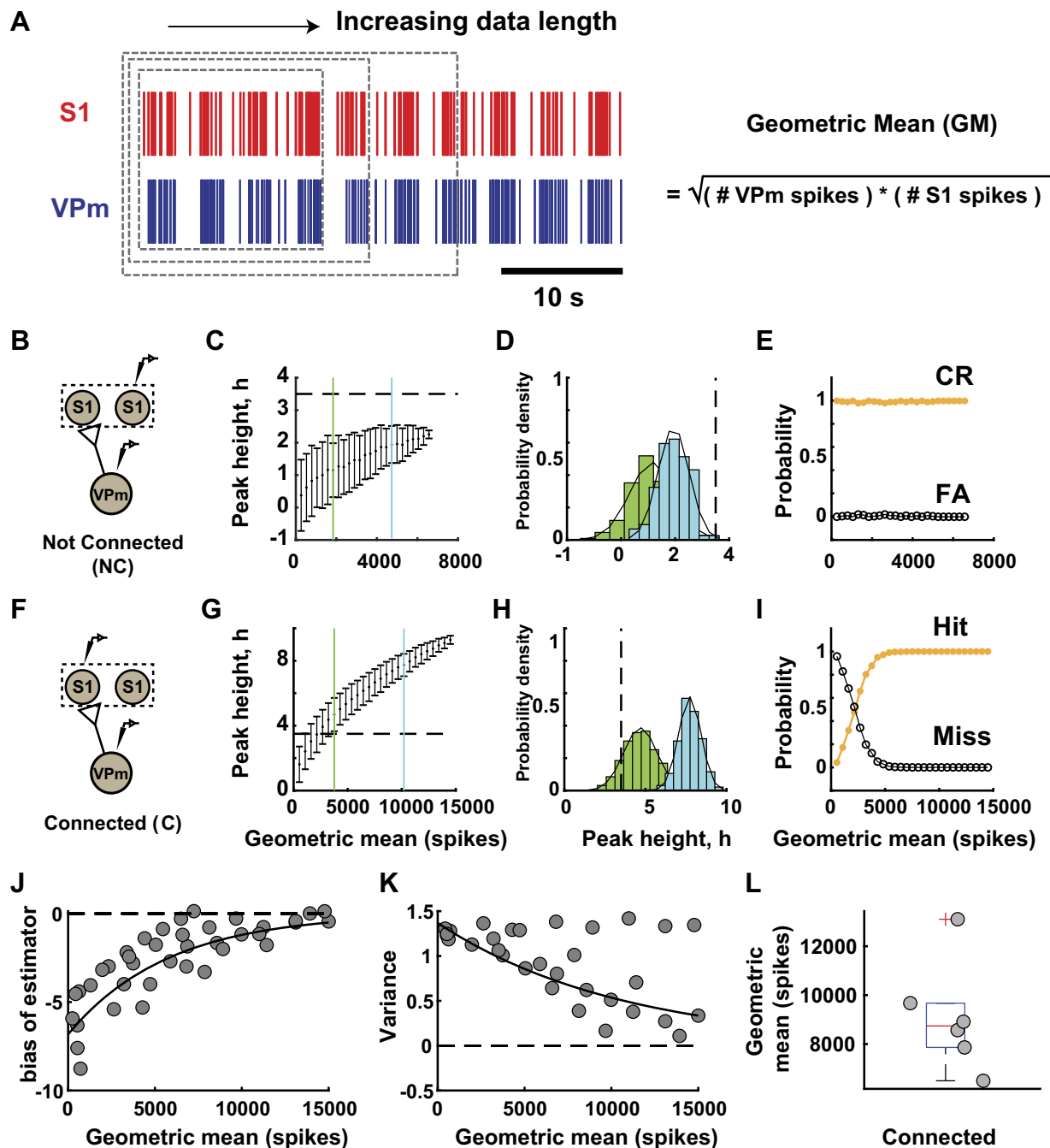


Figure 6. Data length dependence effect on monosynaptic connection inference. **A:** data length dependence effect on connectivity inference was evaluated with a subsampling method. Data length was measured in terms of geometric mean number of spikes, which was calculated by taking the square root of the product of total ventral posteromedial nucleus (VPm) and primary somatosensory cortex (S1) spikes. Random subsampling of the data set was performed in the unit of trials with 1,000 iterations for each condition. **B:** representative example pair of neurons from not-connected distribution in a rat. **C:** mean and standard deviation of peak height from cross correlogram were computed for each subsample of not-connected example. Blue line, short-data length condition (GM: 1,837 spikes); green line, long-data length condition (GM: 4,730 spikes). **D:** distribution of peak height after bootstrapping for 2 data lengths labeled in part I. **E:** probability of outcome for this example. CR, correct reject; FA, false alarm. **F–I:** similar to **B–E** but for connected example in a rat [blue (GM): 3,760 spikes, hit rate 87.7%, miss rate 12.3%; green (GM): 10,201 spikes, hit and miss rates 100%, 0%] (also see Supplemental Fig. S5; see <https://doi.org/10.6084/m9.figshare.14393582.v1>). **J:** bootstrap estimator of bias for each data length. Scatterplot of population data for connected pairs ($n = 6$ pairs, $N = 3$ rats). Solid line, exponential fit ($R^2 = 0.76$). **K:** variance of peak height at each data length for pairs shown in **J**. Solid line, 1st-order polynomial fit ($R^2 = 0.62\%$). **L:** geometric mean for all connected pairs (median: 8,741 spikes, $n = 6$ pairs, $N = 3$ rats).

resulting in a hit rate of 87.7% and a miss rate of 12.3%. We found that the data length required to reach a consistently correct inference was $\sim 5,000$ spikes for this example (Fig. 6J).

From the results in Fig. 6, B–E and F–I (also see Supplemental Fig. S5; see <https://doi.org/10.6084/m9.figshare.14393582.v1>), it appears that data length was critical only for correctly identifying a connected pair and did not

directly affect the inference related to a not-connected pair—in other words, the analysis is prone to type II errors as opposed to type I, and the type II error is strongly dependent upon data length. It is important to point out that the data length needed for sufficiently reducing the probability of error in the inference in Fig. 6J is dependent upon the ground-truth value for the connectivity metric h , as well as the variance in the estimator. We thus analyzed the estimator bias and variance across six connected pairs, as a function of the data length, which we could systematically vary by utilizing subsampling of the full data sets. Figure 6J shows the bias in the estimator for the connectivity metric h , as a function of the geometric mean number of spikes, with generally a negative bias (an underestimate) and a clear exponential decrease in bias with data length as expected, as the full data length is approached. Figure 6K shows the corresponding variance in the estimator of the connectivity metric h , again as a function of the geometric mean number of spikes. Although some of the measures exhibited an apparent invariance to the data length, overall, this quantity decreased exponentially with increasing geometric mean number of spikes, again as expected. For the set of connected pairs of thalamic and cortical neurons here, the geometric mean number of spikes required for the lower bound of resampled data to pass *criterion 2* is shown in Fig. 6L, with a median of $\sim 9,000$ spikes.

Thalamic Synchrony Effects on Monosynaptic Connection Inference

Without having access to the subthreshold activity of the postsynaptic cortical neurons, assessment of connectivity through the co-occurrences of spiking activity in thalamic and cortical neurons often necessitates activation of the intact circuitry with exogenous stimulation because of relatively low intrinsic spontaneous firing rates. The analysis of Fig. 6 revealed a clear motivation for acquiring larger numbers of spikes, which can obviously be facilitated through increased mean firing rates. In sensory pathways, previous studies have used sensory stimuli of varying strengths to evoke higher firing rate in primary sensory areas (12, 14, 20, 23), citing a rule of thumb that involves increasing the number of spikes through external stimulation but not with a stimulus so strong as to induce stimulus-driven synchronization in spiking. Although this approach is logical, it remains ad hoc, and the exact ramifications are not clear. Here, we utilized silicon multielectrode probes in the thalamic VPM and S1 layer IV to quantify changes in neural activity across spontaneous and stimulus-driven conditions and performed analyses to systematically evaluate the potential effects of stimulus-driven changes in firing rate and synchrony on the monosynaptic connection inference between VPM and S1 pairs. Figure 7A shows simultaneous recordings from two thalamic neurons within the same thalamic barreloid and two corresponding cortical S1 neurons in the homologous barrel column. For this example, *VPM unit 1* and *S1 unit 1* were revealed to be connected, whereas *VPM unit 2* and *S1 unit 2* were clearly not connected. Under increasingly stronger stimulus drive, from spontaneous (Fig. 7B, left), to weak sinusoidal whisker stimulus drive (Fig. 7B, center) and to strong repetitive, punctate whisker stimulus drive (Fig. 7B,

right), there is a general increase in firing rate across the recorded cells in both VPM and S1. In addition to the modulation of mean firing rate, we found that increasing stimulus drive affected the inference of connectivity by producing inconsistent conclusions across stimulus conditions, especially obvious with increasingly strong stimuli. Interestingly, we found that this preferentially affected the location of the peak in the cross correlogram, which is associated with *criterion 1* evaluated through the raw cross correlogram. Figure 7C shows the raw and shuffled-corrected spike cross correlograms across the stimulus conditions for the connected pair *VPM unit 1-S1 unit 1*, and Fig. 7D shows this for the not-connected pair *VPM unit 2-S1 unit 2*. Note that we were able to maintain stable recordings for this particular group of neurons over a relatively long experimental time period, enabling us to collect a sufficient number of spikes in the spontaneous condition in order to make inferences regarding connectivity, which we can treat as ground truth here (*VPM unit 1-S1 unit 1* connected, *VPM unit 2-S1 unit 2* not connected). First considering the connected pair *VPM unit 1-S1 unit 1* (Fig. 7C), we found that the inference remained consistent (connected) for spontaneous (I) and sinusoidal (II) stimulus conditions, as it passed both *criteria 1* and *2*. However, for the repetitive transient (III) stimulus condition (Fig. 7C, bottom), although the peak height in the shuffled-corrected cross correlogram exceeded the criterion line (thus satisfying *criterion 2*; Fig. 7C, bottom), there was a disappearance of an isolated peak in the 1–4 ms lag of the raw cross correlogram, which is a violation of *criterion 1*. This led to the incorrect inference of “not connected” for the case of the strong, transient stimulus, or a “miss” in the language of signal detection theory. In our analysis, we have 12 thalamo-cortical pairs for which we have all stimulus conditions, where we consider the spontaneous condition as the ground truth. Of these 12 pairs, 3 pairs were connected (C) and 9 not connected (NC), as determined from the spontaneous condition, which we consider ground truth. For the nine NC pairs, six pairs were incorrectly classified as C in the strong (transient) stimulus case, and the remaining three pairs continued to be correctly classified as NC. For the three C pairs, two pairs were incorrectly classified as NC in the strong (transient) stimulus case, and the remaining pair continued to be correctly classified as C. For this relatively small number of pairs it is difficult to identify a particular pattern in this, but we can generally say that both types of errors can emerge from the strong stimulus that synchronizes the thalamic population, as we also demonstrate in the simulations.

Turning to the not-connected pair *VPM unit 2-S1 unit 2* in Fig. 7D, note that for the spontaneous (I) and sinusoidal (II) case, although the peak height of the shuffled-corrected cross correlogram exceeded 3.5 SD (thus passing *criterion 2*, not shown), we correctly inferred “not connected” for these stimulus conditions given the violation of *criterion 1*. Surprisingly, we incorrectly inferred “connected” for the repetitive transient (III) stimulus condition, as fast peaks emerged in the 1–4 ms lag of the raw cross correlograms, satisfying *criterion 1* (and also *criterion 2*, Fig. 7D, bottom), or a “false alarm” in the language of signal detection theory. We thus encountered two kinds of errors when utilizing exogenous stimulation to increase neuronal firing rates—misses and false alarms—both linked to *criterion 1*,

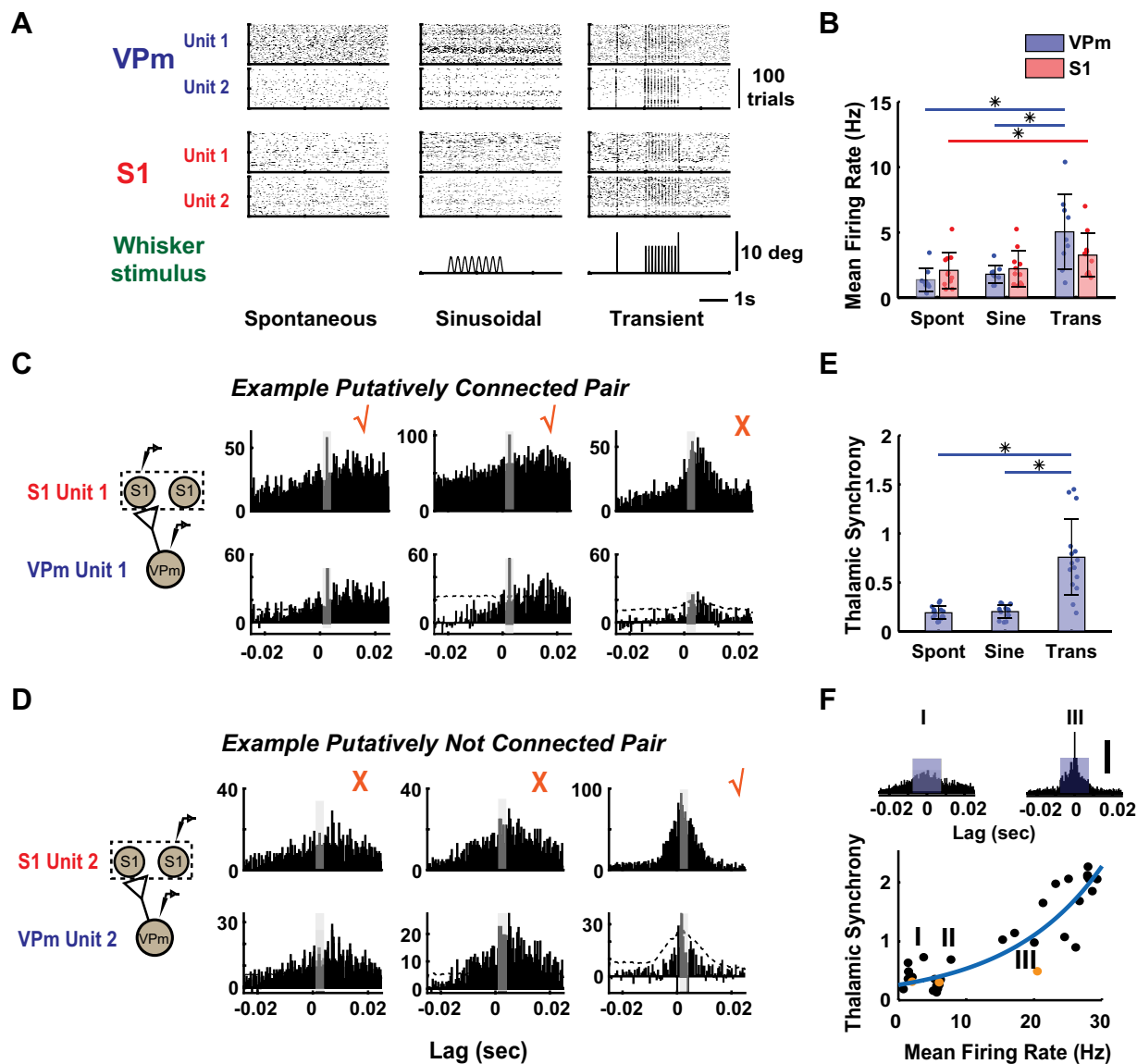


Figure 7. Thalamic synchrony effect on monosynaptic connection inference. **A:** raster plots from simultaneously recorded thalamic and cortical units under spontaneous (no stimulus; Spont), sinusoidal stimulus (mean velocity: $25^\circ/\text{s}$; Sine), and transient inputs ($1,200^\circ/\text{s}$; Trans) in a mouse. S1, primary somatosensory cortex; VPm, ventral posteromedial nucleus. **B:** mean firing rates of thalamus (VPm, blue) and cortex (S1, red) of neuronal pairs were quantified across all 3 stimulus conditions. VPm: spontaneous: 1.38 ± 0.89 Hz, sinusoidal: 2.11 ± 1.37 Hz, transient: 5.05 ± 2.85 Hz; mean \pm SE ($n=9$ neurons); S1: spontaneous: 2.11 ± 1.37 Hz, sinusoidal: 2.23 ± 1.36 Hz, transient: 3.27 ± 1.65 Hz ($n=11$ neurons, $N=1$ mouse) ($*P < 0.05$, Wilcoxon signed-rank test with Bonferroni correction). **C:** monosynaptic connectivity inference for 1 representative example of connected thalamocortical pair from mouse. Checkmark symbols indicate that the pair is being classified as putatively connected; Cross symbols indicate that the pair is being classified as not connected. **D:** same as C but for not-connected example. **E:** thalamic synchrony was computed across 3 stimulus conditions, calculated as number of synchronous events between 2 thalamic units that occur within central window (± 7.5 ms). ($*P < 0.05$, Wilcoxon signed-rank test with Bonferroni correction). Spontaneous: 0.20 ± 0.07 ; sinusoidal: 0.19 ± 0.06 ; transient: 0.76 ± 0.39 ; mean \pm SE ($n=9$ neurons, 15 pairs, $N=1$ mouse). **F, top:** raw spike cross correlograms for the 2 VPm units shown in A (top) in spontaneous and transient stimulus conditions. (I, spontaneous; III, transient). Blue box on each cross correlogram represents the central window (± 7.5 ms) used for thalamic synchrony computation. Scale bar represents 100 spikes in cross correlograms. **Bottom:** the relationship between thalamic synchrony and mean firing rate of respective thalamic pairs was quantified across various stimulus conditions, including spontaneous, sinusoidal, and transient stimuli with 6 different velocities ($n=5$ neurons, 10 pairs, $N=1$ mouse). Orange symbols represent thalamic synchrony across 3 stimulus conditions for example thalamic pair (I, spontaneous; II, sinusoidal; III, transient). Blue line shows exponential fit of the relationship.

due to appearance of spurious peaks in 1–4 ms lag in the cross correlogram.

In previous studies, increase in stimulus-driven firing rate has been shown to couple with higher degree of synchronization within and across neural circuits (14, 46) that can potentially dominate the temporal relationship of the network dynamics revealed by correlational analysis (58). This

highlights the issues underlying the trade-off between firing rate and synchronization of the local network that are intrinsic to the correlational analysis used for monosynaptic connection inference. Several paired recording studies have approached this problem by collecting spontaneous spiking data (13), where presumably the spontaneous activity is less synchronous than stimulus-driven activity, or by providing

weak or nonsynchronizing inputs to probe the circuit (12, 20, 33). However, some degree of synchronization is always present, and a direct understanding of the potential effects and implications of population synchronization of presynaptic neurons on monosynaptic connection inference is lacking. To relate the amount of synchronization across the thalamic units with the increase in stimulus strength, we quantified synchrony using the spike cross correlogram measured across thalamic pairs. Specifically, the synchrony was defined as the number of spikes of the cross correlogram within a window of ± 7.5 ms, normalized by the number of thalamic spikes (see METHODS). Population data showed significant increases in thalamic synchrony comparing spontaneous and transient conditions, as well as sinusoidal and transient conditions (Fig. 7E; $n = 15$ pairs). The raw spike cross correlograms for the two VPM units shown in Fig. 7A, top, are shown in Fig. 7F, top (and orange symbol in Fig. 7F, bottom), illustrating an increase in the central peak of the cross correlogram and thus the thalamic synchrony; note the emergence of sharp peaks from spontaneous to transient stimulus. The nature of the stimulus thus strongly affects the synchrony but also strongly affects the firing rate, suggesting a more general relationship between firing rate and synchrony. To more generally quantify the relationship between thalamic synchrony and mean firing rates, across several experiments we collected thalamic responses to different stimuli [spontaneous, sinusoidal ($25^\circ/\text{s}$), and transient stimuli of different velocities (50, 125, 300, 600, 900, and $1,200^\circ/\text{s}$)], producing a range of firing rates and corresponding degrees of synchrony, displayed in Fig. 7F. In general, there was a monotonic increase in thalamic synchrony with firing rate, fit well by an exponential function (Fig. 7F, blue curve).

To more systematically explore the relationship between the measured thalamic synchrony and *criterion 1* of the thalamocortical connectivity inference, we generated a set of simulations based on experimental data to demonstrate how increasing degrees of thalamic synchrony could influence the connectivity inference. Described in more detail below, the simulations were based on introducing spiking activity that corresponds to varying degrees of synchrony into the experimentally observed spiking activity at the levels of both thalamus and cortex. As described above for experimental observations, through these simulations we also found that the synchronization of the presynaptic thalamic population could potentially produce errors in two scenarios: misses (i.e., a connected pair being incorrectly inferred as not connected, denoted $C \rightarrow \text{NC}$) and false alarms (i.e., a not-connected pair being incorrectly inferred as connected, denoted $\text{NC} \rightarrow C$).

We first sought to simulate the scenario of Fig. 7C, top, where a pair of connected thalamocortical neurons (*VPM unit 1-S1 unit 1*) was misclassified as not connected because a significant maximum peak was not detected in the central 1–4 ms lag of the raw cross correlogram (violating *criterion 1*, Fig. 7C, top right). We hypothesized that this experimental observation was due to a significant increase in cortical firing that was caused by inputs of nearby VPM neurons also connected to the same cortical neuron S1 but relatively synchronous with the reference thalamic neuron *VPM unit 1*. For this simulation, we therefore emulated this scenario by

reintroducing jittered spikes from *VPM unit 1* and *S1 unit 1* back into these data sets, respectively. Importantly, we found from our experimental observations that the mean thalamic and cortical firing rate increased with stimulus strength but cortical firing increased to a lesser extent compared with thalamic firing (not shown). Therefore, the number of added spikes and the jitter (zero-mean Gaussian noise of a specific standard deviation, σ) were both set to produce a specified level of synchrony between the original and perturbed *VPM unit 1* spike train and also match the observed firing rates in both VPM and S1 for this particular condition. The resultant thalamic and cortical activity was denoted as *VPM unit 1** and *S1 unit 1**, respectively. A schematic of this is shown in Fig. 8A. With these manipulations, we performed the analysis of connectivity as before between *VPM unit 1** and *S1 unit 1** at each firing rate level (with corresponding thalamic synchrony level) to generate the probability of the connectivity inference (i.e., probability of satisfying *criterion 1* reported as the fraction of bootstrapped iterations results in satisfying *criterion 1*). We found that the probability of inferring a connection dropped with increasing thalamic synchrony as shown in Fig. 8B, top. For low levels of synchrony (e.g., thalamic synchrony measures of 0.2 or less), the probability of satisfying *criterion 1* (and thus making the correct inference, given that *criterion 2* is satisfied) remained relatively high (from ~ 0.6 to 0.9). However, with increasing levels of thalamic synchrony (and certainly above 0.5), the probability of satisfying *criterion 1* approached 0 (and thus the chance of a miss neared 100%). The raw spike cross correlogram for two synchrony levels (highlighted with green and blue vertical dashed lines) are shown in Fig. 8B, bottom, illustrating the disappearance of the peak in the 1–4 ms lag with increased synchrony. This is consistent with what we observed in the actual experimental data (Fig. 7C, top right). Note that for artificially high levels of synchrony, approaching near-perfect synchrony, the probability of satisfying *criterion 1* does gradually come back up and approach the same probability as for very low levels of synchrony, as expected (not shown for simplicity).

On the other hand, we found that in addition to causing the incorrect classification of a connected pair (i.e., a miss), the thalamic synchrony induced by increased stimulus drive could also have the opposite effect: the incorrect classification of a not-connected pair as connected (i.e., a false alarm). When considering a thalamocortical pair that is not synaptically connected (*VPM unit 2-S1 unit 2*), increased stimulus drive introduces the presence of spiking in the S1 neuron induced by nearby VPM neurons that serve as synaptic inputs to the S1 neuron in question. When these VPM neurons become increasingly synchronous with *VPM unit 2*, this results in the presence of a peak in the raw cross correlogram in the 1–4 ms bin, satisfying *criterion 1* and thus resulting in a false alarm, displayed in Fig. 7E.

For a demonstration of this phenomenon, from experimentally obtained data, we conducted a simple simulation designed to systematically explore this effect. Specifically, in addition to the not-connected pair in question, *VPM unit 2-S1 unit 2*, we identified a distinct, simultaneously recorded thalamocortical pair that was inferred to be connected. By introducing spikes from the connected thalamic and cortical neuron into the spike trains of *VPM unit 2* and *S1 unit 2*,

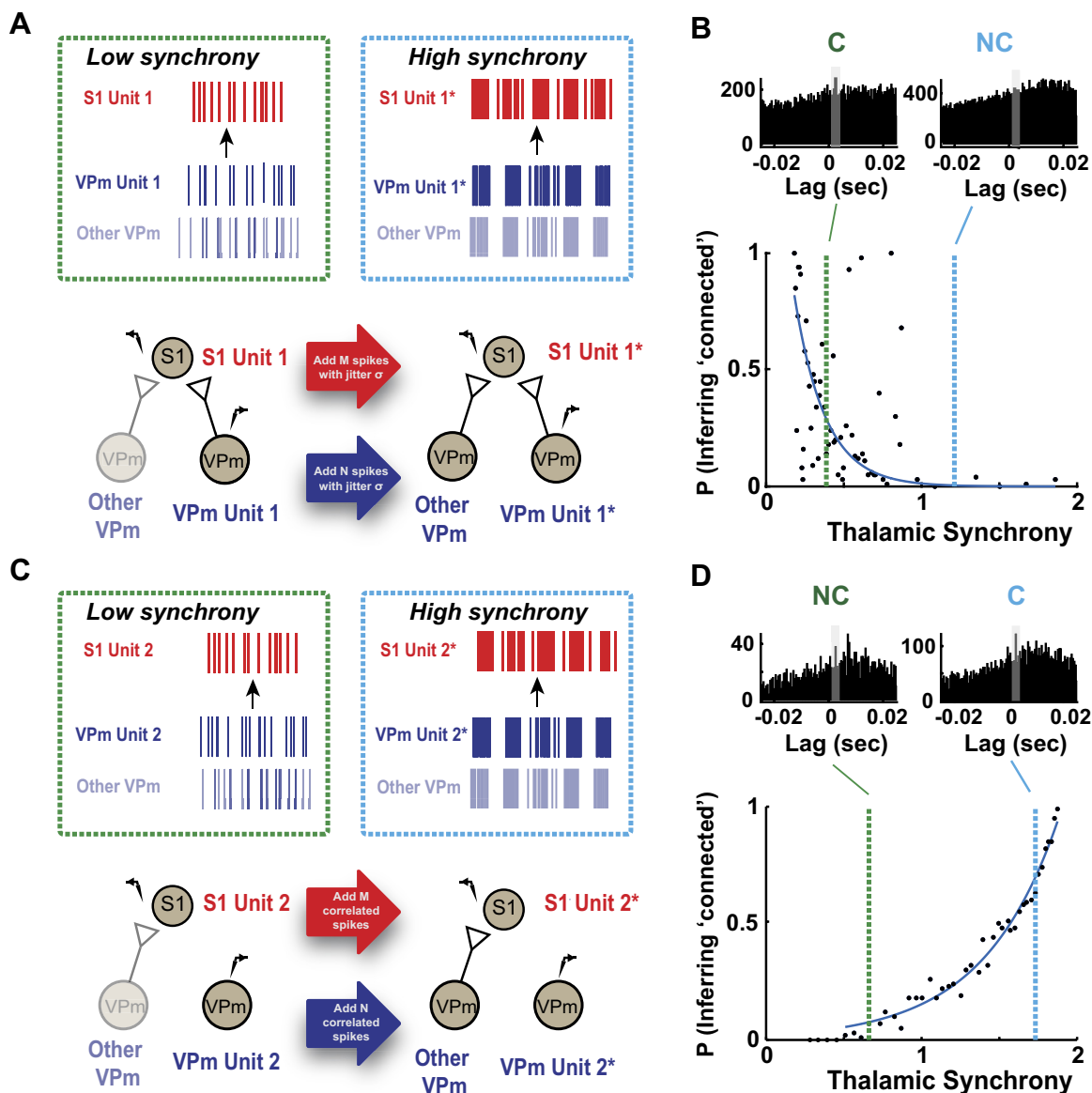


Figure 8. Potential errors in connectivity inference due to thalamic synchrony. **A:** schematic shows conditions for 2 different synchrony levels, low and high. As thalamic synchrony increases, both thalamic and cortical units showed an increase in firing rate accompanied by highly synchronous spiking in the local ventral posteromedial nucleus (VPm) population. To approximate this effect, we gradually added synchronous spikes in VPm and primary somatosensory cortex (S1). We matched the firing rate of thalamic (N spikes) and cortical cells (M spikes), using experimental data, and introduced the same amount of jitter (σ) associated with a specific thalamic synchrony level to both spike trains. **B:** the effects of increase in synchronous firing on the monosynaptic connectivity inference were examined with a probabilistic measure. Our simulation showed that with increasing thalamic synchrony, the probability of satisfying the criterion for monosynaptic connection decreased. Two example raw cross correlograms, corresponding to low and high synchrony level, showed that a connected (C) pair (green, $P = 0.3$ at synchrony level of 0.25) could be misclassified as not connected at a higher synchrony level (light blue, $P = 0.05$ at synchrony level of 1.2). **C:** same as **A** but for an example not-connected (NC) thalamocortical pair. We gradually increased the thalamic and cortical firing by introducing synchronous spikes from a neighboring connected pair (denoted as N correlated spikes for thalamic and M correlated spikes for cortical cell). We found that the probability of error rapidly increased with thalamic synchrony (probability of satisfying *criterion 1* exceeds 0.5 as thalamic synchrony reaches 1.5). **D:** the probability of incorrectly inferring connectivity significantly increased with increasing synchrony. Two example raw cross correlograms at the corresponding thalamic synchrony level showed that a not-connected pair could be misclassified as connected at a higher synchrony level. Note the emergence of monosynaptic peaks in raw cross correlograms with increased synchrony.

respectively, the degree of thalamic synchrony was systematically increased as a function of the number of spikes added but at the same time introduced the presence of cortical spiking from the connected pair. As with the first simulation, the number of spikes added to VPm unit 2 and S1 unit 2

was set to match the observed thalamic and cortical firing rates for this condition, to produce the perturbed spike trains VPm unit 2* and S1 unit 2*. A schematic of this is shown in Fig. 8C. With these manipulations, we performed the analysis of connectivity as before but now between VPm unit 2*

and *S1 unit 2** at each firing level (with corresponding thalamic synchrony level) to generate the probability of the connectivity inference (i.e., probability of satisfying *criterion 1* reported as the fraction of bootstrapped iteration results in satisfying *criterion 1*), as with the first simulation. We found that as thalamic firing became more similar with increasing amount of mixing (reflected in an increase in thalamic synchrony), the raw cross correlogram exhibited the increased likelihood of a peak in the 1–4 ms bin. Correspondingly, the probability of error rapidly increased with thalamic synchrony (probability of satisfying *criterion 1* exceeds 0.5 as thalamic synchrony reaches 1.5 in Fig. 8D, top). The raw spike cross correlogram for two synchrony levels (highlighted with green and blue vertical dashed lines in Fig. 8B), illustrated the appearance of the peak in the 1–4 ms lag with increased synchrony (Fig. 8D, bottom right). Although these simulations should be considered primarily in terms of the basic trends they exhibit, the rapid increase in the probability of error with thalamic synchrony suggests that above some level of synchrony in the presynaptic population, false alarms are inevitable.

DISCUSSION

The field of neuroscience is in a period of rapid tool development, spawned by a combination of innovative technologies and a shift in the focus of international scientific priorities. The explosion of tools for performing large-scale neuronal recording at single-cell resolution provides access to real-time monitoring of network activity within and across multiple brain regions (6, 57, 59). This access enables the exciting potential for interpretation of the causal flow of neuronal activity that ultimately underlies brain function, shaping of perception, and behavior (60). There have been significant efforts in anatomical tracing of connectivity and cell type-specific projections within and across brain regions and hemispheres, leading to new insights into the detailed structure of brain circuits (61). The ultimate goal is to understand how this complex structure gives rise to behaviorally relevant function through the dynamic interaction of neurons within the neural network. However, the identification of functional connections amidst perturbation-induced confounding variables in an intact brain remains very challenging despite increasing accessibility (62). Here, we provided an experimental and analytical framework for quantifying long-range synaptic connectivity that was developed and tested in the thalamocortical circuit of the rodent somatosensory pathway but is generalizable to other circuits and pathways. Importantly, we attacked this from a scalable statistical framework based on signal detection theory, where we established approaches to assess confidence in classification and systematically examined factors contributing to the inference of connectivity.

The gold standard of studying and assessing synaptic connectivity involves direct manipulation of presynaptic neurons to observe a measurable postsynaptic effect. Hence, connectivity studies are often performed with *in vitro* brain slices (63, 64) because of the better accessibility to pre- and postsynaptic neurons concurrently, which is difficult or intractable *in vivo* (31, 65, 66). In attempts to identify connectivity *in vivo*, previous studies have used electrical

stimulation to conduct collision tests that involve comparing the timing of antidromic activation with stimulus-evoked activity to verify origins of projection (43, 67). Although this is a powerful and attractive approach, as it helps to more confidently assess connectivity and establish causal relationships, it does not scale well to assessing connectivity at the population level, where selective stimulation of individual neurons is not typically possible. As an alternative, we adopted non-synchronizing, weak sensory drive (14, 20) to assess likely connectivity through spike cross correlation analysis. Although this approach obviously does not address issues of causality directly, it scales with increasing size of population recordings in the pre- and postsynaptic regions, opening up the possibility for assessing connectivity with large, ensemble recordings (68).

The systematic evaluation of the parameters of analysis presented here offers the potential for the optimization of experiment design for the purpose of assessing connectivity. Although the details likely vary across brain regions and experimental preparations, the results here do suggest some general rules of thumb, perhaps the most important of which revolve around the interplay between data length and synchrony. For example, based on our data, we estimated that ~9,000 spikes (in terms of geometric means of total thalamic and cortical spikes) were needed to reach an inference with high certainty (95% confidence interval) in the fentanyl-anesthetized rat, consistent with the recommended number of spikes used with similar stimulus conditions (14, 33), and between 6,800 and 10,000 spikes for spontaneous and sinusoidal conditions, respectively, in the isoflurane-anesthetized mouse (data not shown). Thus, the requirements were on the same order of magnitude for both of these cases, despite significant differences in experimental preparation (i.e., anesthesia, etc.) and differences in precise anatomical details across the species.

Synchrony across the presynaptic population has long been implicated as a potential confound in assessing synaptic connectivity, typically tied to false alarms (type I error), or the incorrect inference of connectivity in nonconnected pairs (69). The results here supported this long-held assumption, where the artificially elevated synchrony in the VPM population resulted in the increased likelihood of satisfying *criterion 1*, and importantly established ranges of measured synchrony for which this is more likely. Surprisingly, we also found that increased presynaptic synchrony could result in a different type of confound, a miss (type II error), or the incorrect inference of not-connected for connected pairs. Interestingly, this effect emerged over a relatively similar level of synchrony as determined through artificial elevation of the thalamic synchrony. As expected, spontaneous activity is typically fairly asynchronous, and in this regime the types of errors described here are unlikely for this case. However, common drive through sensory input designed to elevate firing in otherwise sparse conditions increases the likelihood of these errors, and thus the trade-off between increased data length and synchronization plays an important role in experimental design. This is further important in extending this approach to awake, behaving conditions, with increased firing rates and continuous modulation in population synchrony by brain state. One alternate explanation for increased likelihood of synaptic connectivity

classification errors as we moved from a stimulus-free condition to highly synchronizing, transient stimuli could be a higher rate of spike sorting errors, where elevated firing across all units (single unit and multiunit) could cause waveform distortion and hence cluster misclassification. Despite a slight reduction in waveform signal-to-noise ratio (4% change for VPM and 1.5% change for S1), however, we found no significant difference when we compared the waveform features of all single units such as peak-to-peak amplitudes and signal-to-noise ratios in spontaneous and stimulus-present conditions (Supplemental Fig. S6, mouse data; see <https://doi.org/10.6084/m9.figshare.14393585.v1>).

Although the approach here was developed with generality in mind, there are several potential limitations related to the specific details of the experimental preparation. First, the data collected in this study were from immobilized, anesthetized rodents. This enabled relatively stable and long-duration recordings of well-controlled stimulus conditions that provided insights for accurate identification of synaptic connectivity across different stimulus regimes. Although we envision the broad applicability of this approach for awake, paired recordings, future experiments are required to pinpoint the optimal experimental conditions for monosynaptic connectivity inference in awake rodents. Specifically, the relationship between mean firing rate and thalamic synchrony must be determined in this context. It was known that the baseline firing rates for both thalamic and cortical neurons are higher under wakefulness (70, 71); however, it is unclear whether thalamic synchrony also increases monotonically with mean firing rate. Additionally, the effect of whisking is likely to confound the relationship between stimulus strength and measured synchrony explored in this study, hence confounding the monosynaptic connectivity inference. However, given the techniques and experimental parameters explored in this study, we believe that this has laid the foundation for capturing connectivity during wakefulness. Ideally, a nonsynchronizing stimulus (sensory or optical) should be used to elevate the mean firing rate across the aligned thalamocortical brain regions, while whisker videography should be in place to record whisker movement. Given that the effects of whisking on thalamic synchrony are unclear and could increase trial-to-trial variability, epochs of whisking should likely be excluded from the analysis for monosynaptic connectivity inference.

Second, the thalamocortical circuit is built on anatomy that is well studied, and highly convergent, with ~50–100 thalamic relay neurons making synapses onto a cortical layer IV neuron with a clear topography (20). This convergent nature of the thalamocortical projections provides significant support in assessing possible connectivity, in contrast to potential connectivity across cortical laminae or other less topographically organized projections. Third, the VPM relay neurons are reported to be uniformly excitatory; thus the presynaptic spiking enhances the likelihood of action potentials in the postsynaptic cortical target. Although long-range projections typically tend to be excitatory rather than inhibitory, analogous approaches should certainly be developed for inhibitory connectivity that is becoming increasingly acknowledged to play a complex and pivotal role in controlling network dynamics (72).

With the scaling up of electrophysiological recordings come challenges. In this work, we performed highly curated, small-scale electrophysiological recordings to evaluate dynamics of VPM (potential presynaptic) and S1 (potential postsynaptic) neurons on a pair-by-pair basis as well as large-scale pre- and postsynaptic recordings, where any pair of neurons from the upstream and downstream structures would be a candidate for connectivity inference. What comes hand in hand with increasing recording yield that enables us to better answer questions about circuit function is an increasing diversity of recording quality, increasing diversity of cell type, and a wide array of possibilities for connectivity. In our hands, we found that the odds of finding putative monosynaptic connections per recording session increased by at least two- to threefold, as illustrated in Fig. 5, where 5–10 single units can be isolated from each brain region for the connectivity inference. Previous studies suggest that high signal quality can be obtained with multisite recording because of its better detectability of extracellular feature across closely spaced contacts (34, 35, 73). Hence, this increase in recording yield as well as the increased probability of detecting monosynaptic connectivity with high-density probe recordings were likely due to improved single unit isolation over time, enabling reliable tracking of single units over longer recording duration (3–4 h). Yet, in practice, handling large amounts of data with probe recordings presents challenges, as most of the spike sorting algorithms to date require manual curation to improve spike classification. This suggests that a certain amount of contamination of spikes from neighboring cells is to be expected. Overall, large-scale recording of neuronal activity will reduce the number of animals and reveal important information only available from monitoring the interaction of brain networks, but the variability inherent in these data sets drives the need for a more comprehensive approach for diverse neuronal ensembles. Traditionally, cross correlation analysis of homogeneous, highly curated, small-scale electrophysiological recordings was primarily used to attach a binary outcome for concluding monosynaptic connection in vivo (12, 13, 19, 33, 44, 74), and data with uncertainties were often discarded. In this work, the evaluation of the neuronal data would not result in a binary classification of connected or not but instead the assignment of a likelihood of connectivity based on the statistical framework we present here, producing a probabilistic connectivity map. Although this approach was developed through analysis of extracellular neuronal spiking data, we also envision that this would be readily adapted to optical imaging approaches that enable cellular resolution calcium or voltage imaging of population spiking activity. Recently, model-based approaches to improve connectivity estimation have been developed for the analysis of large data sets (75–82). These methods typically involve fitting neuronal data or correlational relationships from recordings through models [i.e., generalized linear models (GLMs)] and further aim to reconstruct neuronal circuitry to estimate functional connectivity or to decode causal flow. The statistical approach we present here could eventually be combined with these more structured network modeling approaches to provide a more comprehensive framework for assessing and understanding causal interactions in the brain.

SUPPLEMENTAL DATA

- Supplemental Fig. S1: <https://doi.org/10.6084/m9.figshare.14393528.v1>
 Supplemental Fig. S2: <https://doi.org/10.6084/m9.figshare.14393570.v1>
 Supplemental Fig. S3: <https://doi.org/10.6084/m9.figshare.14393573.v2>
 Supplemental Fig. S4: <https://doi.org/10.6084/m9.figshare.14393579.v2>
 Supplemental Fig. S5: <https://doi.org/10.6084/m9.figshare.14393582.v1>
 Supplemental Fig. S6: <https://doi.org/10.6084/m9.figshare.14393585.v1>

GRANTS

This work was supported by NIH/NIMH Brain Initiative Grant U01 MH-106027 (G.B.S. and C.R.F.) and NIH/NINDS Brain Initiative Grant R01 NS-104928 (G.B.S.). Y.J.L. was supported by the Georgia Tech-Emory-PKU Global Biomedical Engineering Research and Education Fellowship. A.P. was supported by postdoctoral fellowships P300PA_177861 and P2ELP3_168506 from the Swiss National Science Foundation (SNSF). C.J.W. was supported by an NIH NRSA Predoctoral Fellowship (F31NS089412). W.A.S. was supported by an NSF Graduate Research.

DISCLOSURES

No conflicts of interest, financial or otherwise, are declared by the authors.

AUTHOR CONTRIBUTIONS

Y.J.L., C.J.W., and G.B.S. conceived and designed research; Y.J.L. performed experiments; Y.J.L. analyzed data; Y.J.L., A.P., C.J.W., and G.B.S. interpreted results of experiments; Y.J.L. and G.B.S. prepared figures; Y.J.L., A.P., and G.B.S. drafted manuscript; Y.J.L., A.P., C.J.W., W.A.S., C.R.F., and G.B.S. edited and revised manuscript; Y.J.L., A.P., C.J.W., W.A.S., C.R.F., and G.B.S. approved final version of manuscript.

REFERENCES

- Jouhanneau JS, Poulet JF. Multiple two-photon targeted whole-cell patch-clamp recordings from monosynaptically connected neurons in vivo. *Front Synaptic Neurosci* 11: 15, 2019. doi:10.3389/fnsyn.2019.00015.
- Kodandaramaiah SB, Flores FJ, Holst GL, Singer AC, Han X, Brown EN, Boyden ES, Forest CR. Multi-neuron intracellular recording in vivo via interacting autpatching robots. *eLife* 7: e24656, 2018. doi:10.7554/eLife.24656.
- Stoy WA, Kolb I, Holst GL, Liew Y, Pala A, Yang B, Boyden ES, Stanley GB, Forest CR. Robotic navigation to subcortical neural tissue for intracellular electrophysiology in vivo. *J Neurophysiol* 118: 1141–1150, 2017. doi:10.1152/jn.00117.2017.
- Berényi A, Somogyvári Z, Nagy AJ, Roux L, Long JD, Fujisawa S, Stark E, Leonardo A, Harris TD, Buzsáki G. Large-scale, high-density (up to 512 channels) recording of local circuits in behaving animals. *J Neurophysiol* 111: 1132–1149, 2014. doi:10.1152/jn.00785.2013.
- Buzsáki G, Stark E, Berényi A, Khodagholy D, Kipke DR, Yoon E, Wise KD. Tools for probing local circuits: high-density silicon probes combined with optogenetics. *Neuron* 86: 92–105, 2015. doi:10.1016/j.neuron.2015.01.028.
- Jun JJ, Steinmetz NA, Siegle JH, Denman DJ, Bauza M, Barbarits B, et al. Fully integrated silicon probes for high-density recording of neural activity. *Nature* 551: 232–236, 2017. doi:10.1038/nature24636.

- Fiáth R, Raducanu BC, Musa S, Andrei A, Lopez CM, van Hoof C, Ruther P, Aarts A, Horváth D, Ulbert I. A silicon-based neural probe with densely-packed low-impedance titanium nitride microelectrodes for ultrahigh-resolution in vivo recordings. *Biosens Bioelectron* 106: 86–92, 2018. doi:10.1016/j.bios.2018.01.060.
- Raducanu BC, Yazicioglu RF, Lopez CM, Ballini M, Putzeys J, Wang S, Andrei A, Welkenhuysen M, Helleputte N, Musa S, Puers R, Kloosterman F, Hoof C, Mitra S. Time multiplexed active neural probe with 678 parallel recording sites. 2016 46th European Solid-State Device Research Conference (ESSDERC), 2016, p. 385–388.
- Rios G, Lubenov EV, Chi D, Roukes ML, Siapas AG. Nanofabricated neural probes for dense 3-D recordings of brain activity. *Nano Lett* 16: 6857–6862, 2016. doi:10.1021/acs.nanolett.6b02673.
- Nowak L, Bullier J. Cross correlograms for neuronal spike trains. Different types of temporal correlation in neocortex, their origin and significance. In: *Time and the Brain, Conceptual Advances in Brain Research*, edited by Miller R. Amsterdam: Harwood Academic, 2000, p. 53–96.
- Perkel DH, Gerstein GL, Moore GP. Neuronal spike trains and stochastic point processes. II. Simultaneous spike trains. *Biophys J* 7: 419–440, 1967. doi:10.1016/S0006-3495(67)86597-4.
- Reid RC, Alonso JM. Specificity of monosynaptic connections from thalamus to visual cortex. *Nature* 378: 281–284, 1995. doi:10.1038/378281a0.
- Swadlow HA, Gusev AG. The impact of ‘bursting’ thalamic impulses at a neocortical synapse. *Nat Neurosci* 4: 402–408, 2001. doi:10.1038/86054.
- Wang Q, Webber RM, Stanley GB. Thalamic synchrony and the adaptive gating of information flow to cortex. *Nat Neurosci* 13: 1534–1541, 2010. doi:10.1038/nn.2670.
- Lien AD, Scanziani M. Cortical direction selectivity emerges at convergence of thalamic synapses. *Nature* 558: 80–86, 2018. doi:10.1038/s41586-018-0148-5.
- Barthó P, Hirase H, Monconduit L, Zugaro M, Harris KD, Buzsáki G. Characterization of neocortical principal cells and interneurons by network interactions and extracellular features. *J Neurophysiol* 92: 600–608, 2004. doi:10.1152/jn.01170.2003.
- Csicsvari J, Hirase H, Czurko A, Buzsáki G. Reliability and state dependence of pyramidal cell-interneuron synapses in the hippocampus: an ensemble approach in the behaving rat. *Neuron* 21: 179–189, 1998. doi:10.1016/S0896-6273(00)80525-5.
- English DF, McKenzie S, Evans T, Kim K, Yoon E, Buzsáki G. Pyramidal cell-interneuron circuit architecture and dynamics in hippocampal networks. *Neuron* 96: 505–520.e7, 2017. doi:10.1016/j.neuron.2017.09.033.
- Fujisawa S, Amarasingham A, Harrison MT, Buzsáki G. Behavior-dependent short-term assembly dynamics in the medial prefrontal cortex. *Nat Neurosci* 11: 823–833, 2008. doi:10.1038/nn.2134.
- Bruno RM, Sakmann B. Cortex is driven by weak but synchronously active thalamocortical synapses. *Science* 312: 1622–1627, 2006. doi:10.1126/science.1124593.
- London M, Roth A, Beeren L, Häusser M, Latham PE. Sensitivity to perturbations in vivo implies high noise and suggests rate coding in cortex. *Nature* 466: 123–127, 2010. doi:10.1038/nature09086.
- Matsumura M, Chen D, Sawaguchi T, Kubota K, Fetz EE. Synaptic interactions between primate precentral cortex neurons revealed by spike-triggered averaging of intracellular membrane potentials in vivo. *J Neurosci* 16: 7757–7767, 1996. doi:10.1523/JNEUROSCI.16-23-07757.1996.
- Sedigh-Sarvestani M, Vigeland L, Fernandez-Lamo I, Taylor MM, Palmer LA, Contreras D. Intracellular, in vivo, dynamics of thalamocortical synapses in visual cortex. *J Neurosci* 37: 5250–5262, 2017. doi:10.1523/JNEUROSCI.3370-16.2017.
- Yu J, Ferster D. Functional coupling from simple to complex cells in the visually driven cortical circuit. *J Neurosci* 33: 18855–18866, 2013. doi:10.1523/JNEUROSCI.2665-13.2013.
- Ahissar E, Sosnik R, Haidarliu S. Transformation from temporal to rate coding in a somatosensory thalamocortical pathway. *Nature* 406: 302–306, 2000. doi:10.1038/35018568.
- Whitmire CJ, Waiblinger C, Schwarz C, Stanley GB. Information coding through adaptive gating of synchronized thalamic bursting. *Cell Rep* 14: 795–807, 2016. doi:10.1016/j.celrep.2015.12.068.
- Paxinos G, Watson C. *The Rat Brain in Stereotaxic Coordinates*. San Diego, CA: Academic Press, 2007.

28. **Borden PY, Ortiz AD, Waiblinger C, Sederberg AJ, Morrisette AE, Forest CR, Jaeger D, Stanley GB.** Erratum: Genetically expressed voltage sensor ArcLight for imaging large scale cortical activity in the anesthetized and awake mouse. *Neurophotonics* 4: 039801, 2017. doi:10.1117/1.NPh.4.3.039801.
29. **Franklin K, Paxinos G.** *The Mouse Brain in Stereotaxic Coordinates*. Amsterdam: Elsevier Academic Press, 2008.
30. **Lefort S, Tomm C, Floyd Sarria JC, Petersen CC.** The excitatory neuronal network of the C2 barrel column in mouse primary somatosensory cortex. *Neuron* 61: 301–316, 2009. doi:10.1016/j.neuron.2008.12.020.
31. **Pala A, Petersen CC.** In vivo measurement of cell-type-specific synaptic connectivity and synaptic transmission in layer 2/3 mouse barrel cortex. *Neuron* 85: 68–75, 2015. doi:10.1016/j.neuron.2014.11.025.
32. **Constantinople CM, Bruno RM.** Deep cortical layers are activated directly by thalamus. *Science* 340: 1591–1594, 2013. doi:10.1126/science.1236425.
33. **Bruno RM, Simons DJ.** Feedforward mechanisms of excitatory and inhibitory cortical receptive fields. *J Neurosci* 22: 10966–10975, 2002. doi:10.1523/JNEUROSCI.22-24-10966.2002.
34. **Harris KD, Henze DA, Csicsvari J, Hirase H, Buzsáki G.** Accuracy of tetrode spike separation as determined by simultaneous intracellular and extracellular measurements. *J Neurophysiol* 84: 401–414, 2000. doi:10.1152/jn.2000.84.1.401.
35. **Buzsáki G.** Large-scale recording of neuronal ensembles. *Nat Neurosci* 7: 446–451, 2004. doi:10.1038/nn1233.
36. **Fiáth R, Márton AL, Mátyás F, Pinke D, Márton G, Tóth K, Ulbert I.** Slow insertion of silicon probes improves the quality of acute neuronal recordings. *Sci Rep* 9: 111, 2019. doi:10.1038/s41598-018-36816-z.
37. **Storchi R, Bale MR, Biella GE, Petersen RS.** Comparison of latency and rate coding for the direction of whisker deflection in the subcortical somatosensory pathway. *J Neurophysiol* 108: 1810–1821, 2012. doi:10.1152/jn.00921.2011.
38. **Masri R, Bezdudnaya T, Trageser JC, Keller A.** Encoding of stimulus frequency and sensor motion in the posterior medial thalamic nucleus. *J Neurophysiol* 100: 681–689, 2008. doi:10.1152/jn.01322.2007.
39. **Mainen ZF, Sejnowski TJ.** Reliability of spike timing in neocortical neurons. *Science* 268: 1503–1506, 1995. doi:10.1126/science.7770778.
40. **Alonso JM, Martinez LM.** Functional connectivity between simple cells and complex cells in cat striate cortex. *Nat Neurosci* 1: 395–403, 1998. doi:10.1038/1609.
41. **Alonso JM, Usrey WM, Reid RC.** Rules of connectivity between geniculate cells and simple cells in cat primary visual cortex. *J Neurosci* 21: 4002–4015, 2001. doi:10.1523/JNEUROSCI.21-11-04002.2001.
42. **Swadlow HA, Waxman SG, Rose DL.** Latency variability and the identification of antidromically activated neurons in mammalian brain. *Exp Brain Res* 32: 439–443, 1978. doi:10.1007/BF00238715.
43. **Swadlow HA.** Efferent neurons and suspected interneurons in S-1 vibrissa cortex of the awake rabbit: receptive fields and axonal properties. *J Neurophysiol* 62: 288–308, 1989. doi:10.1152/jn.1989.62.1.288.
44. **Swadlow HA.** Fast-spike interneurons and feedforward inhibition in awake sensory neocortex. *Cereb Cortex* 13: 25–32, 2003. doi:10.1093/cercor/13.1.25.
45. **Gil Z, Amitai Y.** Properties of convergent thalamocortical and intracortical synaptic potentials in single neurons of neocortex. *J Neurosci* 16: 6567–6578, 1996. doi:10.1523/JNEUROSCI.16-20-06567.1996.
46. **Temereanca S, Brown EN, Simons DJ.** Rapid changes in thalamic firing synchrony during repetitive whisker stimulation. *J Neurosci* 28: 11153–11164, 2008. doi:10.1523/JNEUROSCI.1586-08.2008.
47. **Gollnick CA, Millard DC, Ortiz AD, Bellamkonda RV, Stanley GB.** Response reliability observed with voltage-sensitive dye imaging of cortical layer 2/3: the probability of activation hypothesis. *J Neurophysiol* 115: 2456–2469, 2016. doi:10.1152/jn.00547.2015.
48. **Millard DC, Stanley GB.** Anatomically based Bayesian decoding of the cortical response to intracortical microstimulation. *2013 6th International IEEE/EMBS Conference on Neural Engineering (NER)*, 2013, p. 1457–1460. doi:10.1109/NER.2013.6696219.
49. **Diamond ME, Armstrong-James M, Ebner FF.** Somatic sensory responses in the rostral sector of the posterior group (POM) and in the ventral posterior medial nucleus (VPM) of the rat thalamus. *J Comp Neurol* 318: 462–476, 1992. doi:10.1002/cne.903180410.
50. **Landisman CE, Connors BW.** VPM and PoM nuclei of the rat somatosensory thalamus: intrinsic neuronal properties and corticothalamic feedback. *Cereb Cortex* 17: 2853–2865, 2007. doi:10.1093/cercor/bhm025.
51. **Sosnik R, Haidarliu S, Ahissar E.** Temporal frequency of whisker movement. I. Representations in brain stem and thalamus. *J Neurophysiol* 86: 339–353, 2001. doi:10.1152/jn.2001.86.1.339.
52. **Castejon C, Barros-Zulaica N, Nuñez A.** Control of somatosensory cortical processing by thalamic posterior medial nucleus: a new role of thalamus in cortical function. *PLoS One* 11: e0148169, 2016. doi:10.1371/journal.pone.0148169.
53. **Sitnikova EY, Raevskii VV.** The lemniscal and paralemniscal pathways of the trigeminal system in rodents are integrated at the level of the somatosensory cortex. *Neurosci Behav Physiol* 40: 325–331, 2010. doi:10.1007/s11055-010-9259-7.
54. **Wright NC, Borden PY, Liew YJ, Bolus MF, Stoy WM, Forest CR, Stanley GB.** Rapid cortical adaptation and the role of thalamic synchrony during wakefulness (Preprint). *bioRxiv* 331660, 2021. doi:10.1101/2020.10.08.331660.
55. **Furuta T, Kaneko T, Deschênes M.** Septal neurons in barrel cortex derive their receptive field input from the lemniscal pathway. *J Neurosci* 29: 4089–4095, 2009. doi:10.1523/JNEUROSCI.5393-08.2009.
56. **Zhang W, Bruno RM.** High-order thalamic inputs to primary somatosensory cortex are stronger and longer lasting than cortical inputs. *eLife* 8: e44158, 2019. doi:10.7554/eLife.44158.
57. **Chung JE, Joo HR, Fan JL, Liu DF, Barnett AH, Chen S, Geaghan-Breiner C, Karlsson MP, Karlsson M, Lee KY, Liang H, Magland JF, Pebbles JA, Tooker AC, Greengard LF, Tolosa VM, Frank LM.** High-density, long-lasting, and multi-region electrophysiological recordings using polymer electrode arrays. *Neuron* 101: 21–31.e25, 2019. doi:10.1016/j.neuron.2018.11.002.
58. **Ginzburg II, Sompolinsky H.** Theory of correlations in stochastic neural networks. *Phys Rev E Stat Phys Plasmas Fluids Relat Interdiscip Topics* 50: 3171–3191, 1994. doi:10.1103/PhysRevE.50.3171.
59. **Ahrens MB, Orger MB, Robson DN, Li JM, Keller PJ.** Whole-brain functional imaging at cellular resolution using light-sheet microscopy. *Nat Methods* 10: 413–420, 2013. doi:10.1038/nmeth.2434.
60. **Sheikhattar A, Miran S, Liu J, Fritz JB, Shamma SA, Kanold PO, Babadi B.** Extracting neuronal functional network dynamics via adaptive Granger causality analysis. *Proc Natl Acad Sci USA* 115: E3869–E3878, 2018. doi:10.1073/pnas.1718154115.
61. **Yuan J, Gong H, Li A, Li X, Chen S, Zeng S, Luo Q.** Visible rodent brain-wide networks at single-neuron resolution. *Front Neuroanat* 9: 70, 2015. doi:10.3389/fnana.2015.00070.
62. **Lepperød ME, Stöber T, Hafting T, Fyhn M, Kording KP.** Inferring causal connectivity from pairwise recordings and optogenetics (Preprint). *bioRxiv* 463760, 2018. doi:10.1101/463760.
63. **Jiang X, Shen S, Cadwell CR, Berens P, Sinz F, Ecker AS, Patel S, Tlomas AS.** Principles of connectivity among morphologically defined cell types in adult neocortex. *Science* 350: aac9462, 2015. doi:10.1126/science.aac9462.
64. **Pfeffer CK, Xue M, He M, Huang ZJ, Scanziani M.** Inhibition in visual cortex: the logic of connections between molecularly distinct interneurons. *Nat Neurosci* 16: 1068–1076, 2013. doi:10.1038/nn.3446.
65. **Jouhanneau JS, Kremkow J, Dorm AL, Poulet JF.** In vivo monosynaptic excitatory transmission between layer 2 cortical pyramidal neurons. *Cell Rep* 13: 2098–2106, 2015. doi:10.1016/j.celrep.2015.11.011.
66. **Jouhanneau JS, Kremkow J, Poulet JF.** Single synaptic inputs drive high-precision action potentials in parvalbumin expressing GABAergic cortical neurons in vivo. *Nat Commun* 9: 1540, 2018. doi:10.1038/s41467-018-03995-2.
67. **Kelly MK, Carvell GE, Hartings JA, Simons DJ.** Axonal conduction properties of antidromically identified neurons in rat barrel cortex. *Somatosens Mot Res* 18: 202–210, 2001. doi:10.1080/01421590120072196.
68. **Juavinett AL, Bekheet G, Churchland AK.** Chronically implanted Neuropixels probes enable high-yield recordings in freely moving mice. *eLife* 8: e47188, 2019. doi:10.7554/eLife.47188.

69. **Ostojic S, Brunel N, Hakim V.** How connectivity, background activity, and synaptic properties shape the cross-correlation between spike trains. *J Neurosci* 29: 10234–10253, 2009. doi:10.1523/JNEUROSCI.1275-09.2009.
70. **Crochet S, Petersen CC.** Correlating whisker behavior with membrane potential in barrel cortex of awake mice. *Nat Neurosci* 9: 608–610, 2006. doi:10.1038/nn1690.
71. **Urbain N, Salin PA, Libourel PA, Comte JC, Gentet LJ, Petersen CC.** Whisking-related changes in neuronal firing and membrane potential dynamics in the somatosensory thalamus of awake mice. *Cell Rep* 13: 647–656, 2015. doi:10.1016/j.celrep.2015.09.029.
72. **Isaacson JS, Scanziani M.** How inhibition shapes cortical activity. *Neuron* 72: 231–243, 2011. doi:10.1016/j.neuron.2011.09.027.
73. **Gray CM, Maldonado PE, Wilson M, McNaughton B.** Tetrodes markedly improve the reliability and yield of multiple single-unit isolation from multi-unit recordings in cat striate cortex. *J Neurosci Methods* 63: 43–54, 1995. doi:10.1016/0165-0270(95)00085-2.
74. **Miller LM, Escabí MA, Read HL, Schreiner CE.** Functional convergence of response properties in the auditory thalamocortical system. *Neuron* 32: 151–160, 2001. doi:10.1016/S0896-6273(01)00445-7.
75. **Chen Z, Putrino DF, Ghosh S, Barbieri R, Brown EN.** Statistical inference for assessing functional connectivity of neuronal ensembles with sparse spiking data. *IEEE Trans Neural Syst Rehabil Eng* 19: 121–135, 2011. doi:10.1109/TNSRE.2010.2086079.
76. **Kobayashi R, Kitano K.** Impact of network topology on inference of synaptic connectivity from multi-neuronal spike data simulated by a large-scale cortical network model. *J Comput Neurosci* 35: 109–124, 2013. doi:10.1007/s10827-013-0443-y.
77. **Kobayashi R, Kurita S, Kurth A, Kitano K, Mizuseki K, Diesmann M, Richmond BJ, Shinomoto S.** Reconstructing neuronal circuitry from parallel spike trains. *Nat Commun* 10: 4468, 2019. doi:10.1038/s41467-019-12225-2.
78. **Lütcke H, Gerhard F, Zenke F, Gerstner W, Helmchen F.** Inference of neuronal network spike dynamics and topology from calcium imaging data. *Front Neural Circuits* 7: 201, 2013. doi:10.3389/fncir.2013.00201.
79. **Okatan M, Wilson MA, Brown EN.** Analyzing functional connectivity using a network likelihood model of ensemble neural spiking activity. *Neural Comput* 17: 1927–1961, 2005. doi:10.1162/0899766054322973.
80. **Paninski L, Pillow JW, Simoncelli EP.** Maximum likelihood estimation of a stochastic integrate-and-fire neural encoding model. *Neural Comput* 16: 2533–2561, 2004. doi:10.1162/0899766042321797.
81. **Stevenson IH, Rebesco JM, Miller LE, Körding KP.** Inferring functional connections between neurons. *Curr Opin Neurobiol* 18: 582–588, 2008. doi:10.1016/j.conb.2008.11.005.
82. **Zaytsev YV, Morrison A, Deger M.** Reconstruction of recurrent synaptic connectivity of thousands of neurons from simulated spiking activity. *J Comput Neurosci* 39: 77–103, 2015. doi:10.1007/s10827-015-0565-5.
83. **Baião PdAA.** *Nanostructuring Silicon Probes via Electrodeposition: Characterization of Electrode Coatings for Acute in vivo Neural Recordings* (dissertation). Lisbon: Faculdade de Ciências e Tecnologia, Universidade Nova de Lisboa, 2014.